The Reconstruction of High-p_T Photons with the Electromagnetic Calorimeter of the ALICE Experiment at the LHC

Heather M. Gray

November 17, 2005

In memory of Tifaine James

Abstract

In two years, the frontier of relativistic heavy ion physics will move to the Large Hadron Collider (LHC), which will explore matter with energy densities greater than 10 times that at the Relativistic Heavy Ion Collider (RHIC), providing an opportunity to test predictions of Quantum Chromodynamics (QCD). At the LHC, the cross-sections for high momentum processes are expected to be sufficiently large for jet physics to play an important role. Some first hints of this exciting physics have already been reported at RHIC energies, namely observation of jet quenching, as indicated by the suppression of the yield of high p_t hadrons and the suppressed yield of back-to-back correlated hadrons from jets, in central Au+Au collisions.

However, careful jet and jet quenching analyses require calibration with the parton energy prior to its passage though the nuclear matter. This can only be obtained via analysis of γ-jet processes because photons, once produced, are essentially unaffected by a colour-charged medium, and pass through the medium retaining their original energy. The experimental challenges include identifying photons within the high multiplicity heavy-ion environment and reducing the background from the photonic decays of neutral pions.

This thesis details algorithms developed for photon reconstruction in the heavy ion environment for the electromagnetic calorimeter (EMCal) of the ALICE experiment. Shower shape analysis was used to optimise cuts to discriminate between the direct photon signal and the background from the photonic decays of neutral pions. Photon energy resolution of approximately 5% at 10 GeV and 3% at 30 GeV was obtained in simulations. An enhancement in the γ/π^0 ratio by a factor of 50 relative to theoretical predictions at 20 GeV was obtained using the techniques of shower shape analysis.

Acknowledgements

Thank you to everybody who has contributed one way or another to this work, especially those I have neglected to mention here.

Thank you to Professor Cleymans for being such a supportive supervisor and organising many exciting opportunities for me. Thank you to Grazyna Odyniec for being my second (unofficial) supervisor, for teaching me about physics and improving my scientific writing. Thank you to Marco van Leeuwen for having gone far out of his way to assist me with my work and for always answering my questions, even late at night.

I am indebted to Peter Hristov for introducing me to ROOT and AliROOT, and for supervising my work at CERN.

It has been great working with the ALICE and ALICE-USA collaborations. I'd especially like to thank Terry Awes for teaching me about photons and for taking an avid interest in my work and Mark Horner for helping me with AliROOT and Linux. Thank you also to Tom Cormier, Andreas Morsch, Yves Schutz, Gustavo Conesa, Sarah Blyth and Aleksei Pavlinov for many fruitful discussions.

It has been great to have been a member of the UCT-CERN Research Centre. Thank you to Peter Steinberg for introducing me to the field of experimental heavy-ion physics.

I was fortunate to spend time in the LBL-RNC group in Berkeley. I'd like to thank the LBL staff, postdocs and students for buying me many, many espressos and for always being willing to answer questions.

SPIRES (http://www.slac.stanford.edu/spires/) and google (http://www.google.com) have provided invaluable help in tracking down papers and citations. Thank you also to the Smashing Pumpkins and Radiohead for making the writing of this thesis a less painful experience.

I would like to thank Lawrence Berkeley National Laboratory and CERN for their hospitality. Funding from the National Research Foundation (NRF) and the University of Cape Town is much appreciated.

Thank you to Grazyna, Marco, Sam, Sarah and Mark for the care with which you proofread this thesis. Any remaining mistakes are mine, not theirs.

Lastly, I like to thank those people close to me. Thank you to my friends, real and virtual, for their support and companionship, especially: Aras, Caitlin, Kat, Lisa, Michelle, Natacha, Olly, Sam and all the Chateauvians. Thank you to my family for your support, love and many plane tickets over the years.

Contents

Chapter 1

Introduction

High-energy nuclear collisions are used to study matter under extreme conditions with high temperatures and pressures possibly leading to the formation of a new state of matter, the Quark-Gluon Plasma (QGP). At low temperatures the basic constituents of matter, quarks and gluons, are confined inside nucleons by the strong interaction, but at high temperatures a phase transition to a plasma of deconfined quasi-free quarks and gluons, the QGP, is expected.

Photons do not carry the colour charge of the strong interaction and therefore do not interact as they pass through a colour-charged medium. In γ-jet production, a photon and a parton are produced in a hard scattering, with identical energy but opposite direction. The hard parton is expected to interact with the medium and lose energy, but the photon will emerge with its original energy. Measurement of the energy of both the photon and the jet formed by the fragmentation of the parton, will determine parton energy loss in the medium.

This thesis explores detection techniques for high transverse momentum photons in high-energy nuclear collisions at the LHC, using the proposed electromagnetic calorimeter of the ALICE experiment.

The thesis is structured as follows. Chapter 2 motivates the study of high-energy nuclear collisions, highlighting photon production mechanisms. The experimental setup is discussed in Chapter 3. Chapter 4 introduces the simulation software and clusterisation techniques. Technical work to improve the simulation and cuts to reduce background are discussed in Chapter 5. Chapter 6 presents the results obtained for photon energy resolution measurements and the use of shower shapes to discriminate between photon and neutral pion showers. A discussion of algorithm improvements and physics measurements concludes this thesis.

Chapter 2

The Search for the Quark-Gluon Plasma

The nature of the fundamental constituents of the world has puzzled philosophers for many centuries. Over time, the answer has evolved from atoms, through nuclei [1] to neutrons [2] and protons [3] and finally to the current hypothesis: quarks. Quarks were first proposed by both Gell-Mann and Zweig in 1964 [4] to explain the observed structure in hadron quantum numbers [5].

Four fundamental forces governing the behaviour of matter have been identified: gravity, the electromagnetic force, the strong nuclear force and the weak nuclear force. Some, or perhaps all, of these forces become unified at high-energies. Each force, except possibly gravity, is mediated by an exchange particle with the interaction strength determined by a coupling constant. The theory of the strong nuclear force, Quantum Chromodynamics (QCD), describes the interactions between quarks as mediated by the exchange of gluons.

Even though the existence of quarks has been postulated for a long time, quarks have never been observed in isolation (see [6] for reviews). This is attributed to the strength of the strong interaction and known as *confinement* [7]. However, at the high-energies of accelerator experiments, the strong interaction is also described successfully by the parton model [8] in which the inter-quark interaction is weak. This behaviour at high energies or small distances is known as asymptotic freedom [9, 10].

Current cosmological theories state the universe was created through the Big Bang [11]. The universe was initially filled with quickly expanding and cooling radiation. By approximately 1 μs the temperature and energy density had dropped sufficiently so that quarks and gluons condensed out of the energy cloud. This "soup" of free quarks and gluons is thought to have existed until 10 μs when the quarks and gluons coalesced into hadrons. The state of matter with quarks and gluons free to move over distances greater than a nucleon has come to be known as the Quark-Gluon Plasma (QGP).

2.1 QCD, Lattice QCD and the QCD Phase Diagram

The primary difference between QCD and the theory of electromagnetism, Quantum Electrodynamics (QED), is that there is a strong interaction between the gluons. A field theory with quanta that are themselves a source of the field is non-Abelian. The non-Abelian nature of QCD causes the coupling to decrease at small distances [9], precisely the opposite to QED. At these small distances a perturbative treatment of QCD can be used (see Section 2.4). In contrast, when probing large distances, such as the structure of the hadron ground state, the coupling constant is large and perturbation theory cannot be applied.

The MIT bag model [12] provides a phenomenological description of quarks confined within a hadron. In this model, quarks are described as massless particles when within the bag and infinitely massive when outside it. They are confined to the bag by a parameter called the *bag pressure*, which accounts for non-perturbative aspects of QCD. With the increase of

temperature, the pressure from the quark matter increases (due to the increase in the number of quarks in the bag as well as their kinetic energy) until it exceeds the bag pressure and becomes deconfined. Increasing the density of quarks within the bag lowers the deconfinement temperature, as shown in the QCD phase diagram (Figure 2.1).

The QCD phase diagram shows the relation between temperature, T, and baryonic chemical potential[1], μ_B [13]. Ordinary matter, with $\mu_B = m_{proton}$, occurs at low temperature, as indicated by the grey semicircle. The deconfinement transition is represented by the line in the diagram. The blue arrow indicates the path followed by the cooling universe on the phase diagram, characterised by equal proportions of matter and antimatter, i.e. $\mu_B \approx 0$. Other exotic states of matter are predicted to occur at low temperature and high baryon density such as colour-superconductivity within neutron stars.

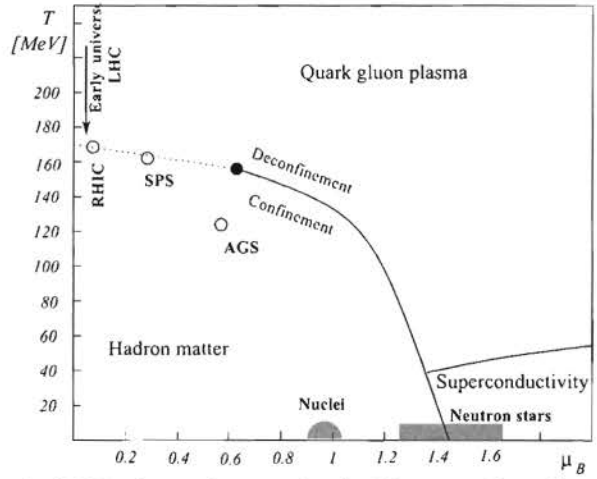

Figure 2.1: Schematic QCD phase diagram in the $T - \mu_B$ plane from [14]. At low T and μ_B nuclear matter is confined with hadrons as the degrees of freedom. At higher T a phase transition to a deconfined QGP is indicated by a line. The phase diagram is predicted to have a critical point, the precise location of which is unknown. Exotic quark phases may occur at high density, such as superconductivity within neutron stars. Possible conditions at chemical freeze out at AGS, SPS and RHIC are indicated with blue circles. The blue arrow indicates the expected evolution of the early universe and a similar path is expected to be reproduced by LHC collisions.

Lattice gauge theory is a more sophisticated non-perturbative treatment of QCD and uses a discrete lattice of space-time coordinates [7] to calculate the transition temperature and energy density. An example of recent lattice QCD results, the dependence of ϵ/T^4 on the temperature with $\mu_B = 0$, is shown in Figure 2.2 [15] . The red and blue lines show calculations using two and three light quark flavours respectively, while the light blue line uses two light and one heavy quark mass, representing the light up and down quarks and the heavier strange quark. At the critical temperature, $T_c = 173$ MeV, ϵ/T^4 increases suddenly due to the phase transition, although this rise is more gradual in the 2+1 flavour case. The ideal gas limit, indicated by an arrow on the vertical scale, is never completely reached even at four times the critical temperature.

Recent lattice QCD calculations at finite baryon density have predicted a critical point in the $T - \mu_B$ plane [16], located at the change from an analytical crossover to a first order

[1]The baryonic chemical potential is a measure of the excess of baryons over anti-baryons in a system. μ_B is shown in units of nuclear density, in which $1 = m_{proton} = 940$ MeV

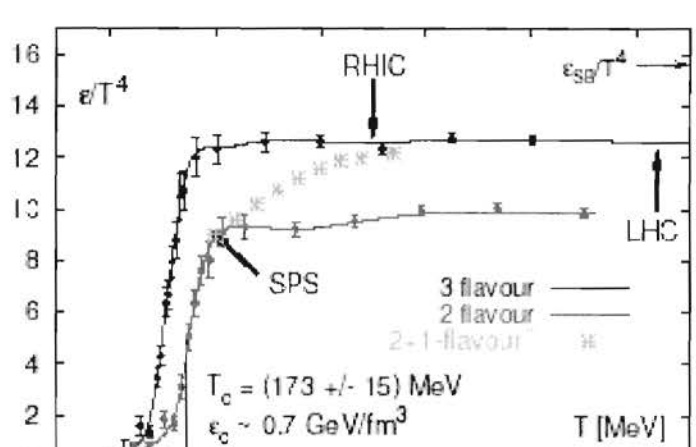

Figure 2.2: The energy density as a function of temperature for lattice calculations using different numbers of quarks [15]. The two and three flavour lines are calculations for two and three light quarks. The two plus one flavour line is a calculation using two light quarks and one heavy quark. The arrows on the right show the value calculated for the Stefan-Boltzmann limit for an ideal gas.

transition, although the precise transition orders are still under discussion. Calculations of the critical point with physical quark masses have predicted it to be located at $T_E = 162 \pm 2$ MeV and $\mu_E = 36 \pm 40$ MeV, as shown in Figure 2.3 [17]. Large fluctuations are expected to be observed in systems near the critical point, resulting in recent experimental efforts.

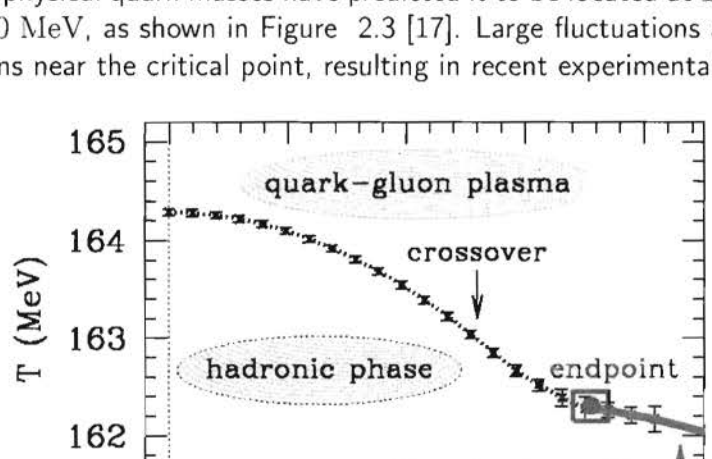

Figure 2.3: Lattice QCD calculation of the critical point [16,17] position in the QCD phase diagram. The errors shown are only those from the reweighting process and, together with an additional 1.3% error from the scale determination at T=0, the location is calculated as: $T_E = 162 \pm 2$ MeV and $\mu_E = 360 \pm 40$ MeV

A theory requires experimental confirmation. QCD predicts the existence of a deconfined phase of matter therefore it is desirable to observe it. The Big Bang is unrepeatable but by colliding heavy nuclei together at high energies, very large energy densities can be obtained in the laboratory, reproducing conditions similar to those that occurred in the Big Bang. We

now briefly outline the history of heavy-ion collisions.

2.2 Heavy-ion collisions

In 1974, T.D. Lee suggested at the workshop on "BeV/nucleon Collisions of Heavy-Ions" at Bear Mountain, New York that it would be interesting to explore new phenomena "by distributing high energy.. over a...large volume" to restore the broken symmetries of the vacuum and create abnormal states of dense matter [18]. At the same meeting, W. Greiner suggested that high energy densities could be achieved with relativistic heavy-ion collisions. In 1975, Collins and Perry [19] realised that asymptotic freedom in QCD might imply the existence of an ultra-dense form of matter with deconfined quarks and gluons [13], first called the Quark-Gluon Plasma (QGP) by Shuryak [20, 21].

The experimental program in nucleus-nucleus collisions began in the mid-1970s at the LBL Bevatron-Bevalac facility using fixed target experiments and beams with energies up to 2 GeV per nucleon. It continued through the 1980s and 1990s with fixed target experiments at the Alternating Gradient Synchrotron (AGS), with $\sqrt{s} = 2.5 - 5$ GeV and the Super Proton Synchrotron (SPS) , with $\sqrt{s} = 17.3$ GeV, at Brookhaven and CERN respectively. In 2000, the Relativistic Heavy Ion Collider (RHIC) at Brookhaven recorded the first collisions of two Au+Au beams. Today RHIC has reached an energy of $\sqrt{s} \approx 200$ GeV per nucleon. The Large Hadron Collider (LHC) is scheduled to begin colliding Pb-ion beams in 2008 with $\sqrt{s} \approx 5.5$ TeV per nucleon. For recent reviews of high-energy nuclear physics experiments, see [22].

Heavy ion collisions are visualised in the centre-of mass frame as the collision of two Lorentz-contracted disks. The stages of the collision evolution (Figure 2.4), in a simplified picture [23], are as follows. In the *pre-equilibrium* phase the nucleons pass through each other undergoing partonic interactions. A fire-ball of quarks and gluons forms at mid-rapidity and equilibrates through rescattering in about 1 fm. This thermalised fire-ball is the QGP stage and it evolves hydrodynamically. The rapidly expanding and cooling QGP quickly reaches *chemical freeze-out*, the temperature at which the hadron abundances are determined. This hadronic gas cools further until *thermal freeze-out* after which the particles no longer scatter off each other and the momentum distribution is fixed. See [24] for further discussion.

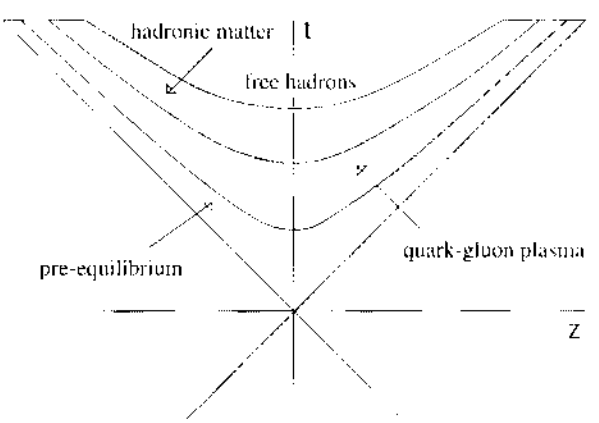

Figure 2.4: A space-time diagram for the evolution of a heavy-ion collision [25]after [23]

2.3 Detecting the QGP

The transient existence of the QGP means that its presence can only be inferred by careful analysis of the particles after hadronisation. A number of signatures for QGP formation have

been proposed, of which a few will be outlined here. The reader is referred to [22] for a full discussion.

- Low energy leptons and photons emitted by the medium were expected to measure the temperature of the matter produced in high-energy nuclear collisions [26]. A small dilepton excess has been observed at the SPS [27] and attributed to thermal emission [28], but the measurements are limited by statistics. Photon production and detection will be discussed further in Section 2.5.

- Colour screening in the QGP was expected to melt the J/Ψ particle leading to suppression relative to p+p collisions [29]. J/Ψ production was observed to be increasingly suppressed with centrality in nucleus-nucleus collisions at the SPS [30], but the suppression observed in p+A collisions has raised doubts about the interpretation. Measurements of J/Ψ production at RHIC are currently statistics limited, but results are expected soon.

- Enhanced strangeness production was one of the first signals of QGP formation to be proposed [31]. Strangeness production is suppressed in elementary hadronic collisions [32] because of the mass difference between strange and light hadrons. In a deconfined medium the mass of the strange quark is reduced as it changes from a constituent quark to a current quark. This mass reduction was expected to restore strangeness production to the levels predicted by hadron resonance models. Strangeness enhancement has been observed in nucleus-nucleus collisions but, until recently, there was no dramatic change with increasing energy. A dramatic change in strangeness fluctuations with energy has been reported by NA49 [33], but the interpretation of the data is still under discussion. See [34] for a recent review of strangeness production.

- A high-energy parton passing through a QGP was expected to lose energy by interacting with the colour charged medium. This phenomenon, also known as jet quenching, has been observed at RHIC and will be discussed further in Section 2.4.

- Momentum anisotropies were expected to provide a measure of the density and pressure of the medium [35]. In contrast to what was observed at SPS, the strength of elliptic flow at RHIC has been striking and reached the hydrodynamic limit [36].

2.4 Hard Probes

A hard probe is created in a momentum transfer significantly larger than the typical scale of QCD, Λ_{QCD}, therefore its production cross-section can be calculated using a perturbative expansion of the strong coupling constant, α_S. The terms of the perturbative series can be visualised with Feynman diagrams, with each vertex in the diagram contributing a factor of $\sqrt{\alpha_S}$ to the matrix element. The order of the calculation refers to the maximum order in α_S included. Currently pQCD calculations extend to the next-to-next-to-leading order (NNLO), which includes terms up to α_S^4.

Hard probes are produced very early in the collision and hence probe the partonic phase directly. The initial production yield can be calculated using perturbative QCD and compared to vacuum production by scaling p+p results by the number of binary inelastic collisions. Typical hard probes include high-p_T hadrons, jets, direct photons and hadrons containing heavy flavours.

The study of parton energy loss began with a suggestion from Bjorken, in 1982, that a hard parton traversing a QGP would suffer *collisional energy loss* via elastic scatterings [8]. Later it was shown that *radiative energy loss* was larger [37] than this collisional energy loss.

The theoretical development of parton energy loss continued with the introduction of the non-Abelian analogue of the LPM (Landau, Pomeranchuk and Migdal) effect [38] to model multiple scattering with a screened Coulomb potential [39]. BDMPS (Baier, Dokshitzer, Mueller, Peigé and Schiff) later showed that gluon rescattering is very important in a dense medium [40] and that parton energy loss depends on the size of the medium, L. Recent works on parton energy loss include a path integral approach [41], twist [42] and an opacity expansion framework [43]. For a contemporary summary of the theory of parton energy loss, see [44].

High-p_T hadron suppression is one of the most striking observations at RHIC (Figure 2.5) [45–47]). It has been interpreted as being caused by strong initial state effects, such saturation of the small-x gluon densities [48], and final state effects, including fragmentation function modification and parton energy loss, as discussed above, but after d+Au measurements of high-p_T hadrons were consistent with p+p results (Figure 2.5), the suppression has usually been interpreted as a final state effect.

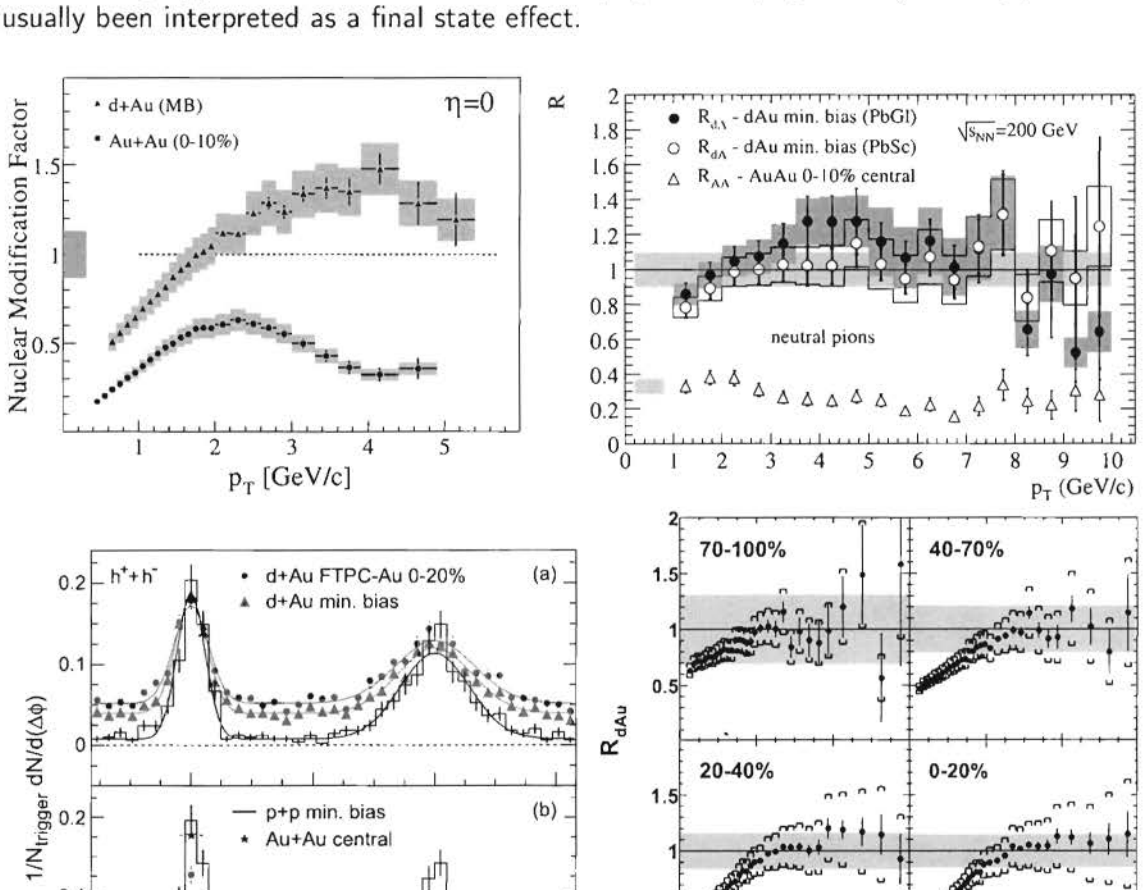

Figure 2.5: Binary collision-scaled ratio of charge hadron and π^0 inclusive spectra from 200 GeV Au+Au and d+Au data relative to that from p+p collisions from BRAHMS [45] (upper left), PHENIX [46] (upper right) and PHOBOS [47] (lower right). Di-hadron azimuthal correlations at high p_T for p+p, d+Au and Au+Au collisions with background subtraction (lower left) from STAR [49].

Because hadron spectra have limited sensitivity to the properties of the medium [50], the next logical step would be full jet reconstruction. Jets are reconstructed in high-energy nuclear

collisions by summing the energy in a cone centred on the jet axis. In-medium energy loss has been shown to proceed via collinear gluon radiation [51]. These collinear gluons are emitted within the jet cone so that the total jet energy is unaltered even when it passes through a medium. Additionally, energy resolution measurements are limited by large event-to-event background fluctuations [52].

Jet fragmentation functions, following their study in e^+e^- and p+p collisions [53] have been proposed to measure parton energy loss, because the momenta of the particles in the jet will be reduced by passing through a medium. Fragmentation functions are defined for p+p collisions as:

$$D(z) = \frac{1}{N_{jets}} \frac{dN_{ch}}{dz} \tag{2.1}$$

where

- N_{ch} = number of charged particles
- $z = \frac{p_L}{E_T}$
- p_L = particle momentum parallel to the jet axis
- E_T = transverse jet energy

Wang et al [54] proposed that the energy of a photon emitted in the opposite direction to the jet (in the γ-jet process), could be used to measure the original jet energy. This proposed measurement is the primary motivation for this thesis, and we shall return to the topic in more detail after discussing photon production mechanisms.

2.5 Photons

Photons have long been considered to be a gold-plated probe of QGP formation [21, 55] because they only interact electromagnetically and have a mean-free path much larger than the fireball. Therefore they pass through the fireball, without interaction, preserving information from their creation time.

The photon production mechanisms thought to occur in heavy-ion collisions are summarised in Figure 2.6. Photons produced at early stages of the system evolution are termed *direct photons*, to distinguish them from *decay photons* produced in electromagnetic meson decays. Decay photons are mainly an experimental problem albeit far from trivial. Discrimination between direct and decay photons is the central topic of this thesis, but first the different direct photon production mechanisms will be discussed. Direct photon production in high-energy nuclear collisions includes *QCD-based production*, calculated with p+p pQCD and scaled by the number of inelastic binary collisions, and *medium-induced production* in which photons are produced by the hot dense medium.

Direct photon production in p-i p collisions has been calculated in pQCD at the next-to-leading order[2] (NLO). The direct photon cross-section is the sum of *prompt* and *bremsstrahlung* components. Prompt photons predominantly come from gluon Compton scattering, when an incoming quark absorbs a gluon and then emits a photon (Figure 2.7(a)) and quark-antiquark annihilation, illustrated in Figure 2.7(b). Bremsstrahlung photons are produced in calculable processes, such as a quark radiating off a photon (Figure 2.7(d)) and during parton fragmentation into hadrons (Figure 2.7(e)).

[2]The order of a pQCD calculation refers to the powers in α_s considered. NLO pQCD calculations include terms up to α_s^4

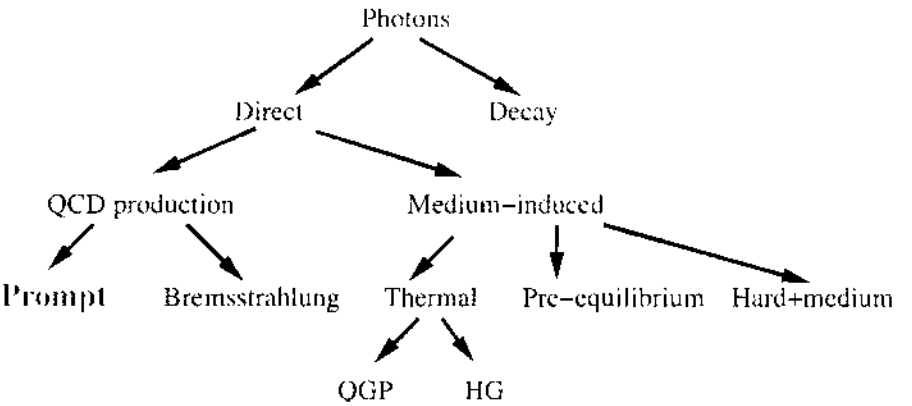

Figure 2.6: Photon production mechanisms in heavy-ion collisions. Adapted from [56]

Perturbative QCD calculations have intrinsic uncertainties due to the arbitrary choice of renormalisation, factorisation and fragmentation scales resulting in uncertainties in the predicted photon p_T-spectra of around 20-30%. In comparisons to p+p data, the calculated p_T spectra are systemically less steep and are depleted at low p_T. A phenomenological parameter used to represent initial state momentum broadening, k_T, improves the agreement to the data.

In heavy-ion collisions there are additional direct photon sources due to the hot dense medium (see Figure 2.6). These include *pre-equilibrium photons* [57], produced during the thermalisation of the fireball; *thermal photons*, produced in collisions of the quarks and gluons in the medium, and *hard+medium*, produced by a hard parton interacting with the thermal partons in the medium.

Thermal photons are produced during both the QGP, if present, and the Hadron Gas (HG) phases and their momentum distribution reflects that of the particles that produced them. There has been much debate over whether the photons from the QGP will outshine those from the HG, or vice versa. Initially, Hwa and Kajantie predicted that thermal production in a QGP would be greater than in a HG at the same temperature [58], but later Kapusta et al [59] argued, on general grounds, that photon production depended on the temperature, not the phase of matter. The following year, 1992, Xiong et al [60] calculated that photon production rates through the a_1 resonance exceeded those considered by Kapusta et al. Complete leading order results for photon emission in a QGP [61] have recently been compared to the latest HG thermal photon calculations, with revised a_1 production [62, 63]. These calculations show that at RHIC energies the QGP thermal photon production outshines the HG for photons with energies between 1 and 3 GeV, but that there is no energy range where this occurs at SPS. It is thought that there may be additional effects on thermal photon production when non-zero baryon density is used in the calculations.

Direct photons are also produced in interactions between a hard parton and the medium, such as a fast parton interacting with a thermalised QGP parton [64] and induced photon bremsstrahlung from multiple scattering of a fast quark in a QGP [65]. Figure 2.8(b) compares the contributions to high-p_T photons from the different sources [63]. At energies below 17 GeV the photons produced in the interactions between jets and thermal partons (red) are the dominant direct photon source, after which the prompt photons (blue) dominate. At RHIC, in contrast, the NLO pQCD photons are the largest contribution for $p_T > 5$ GeV.

2.5.1 Measuring Direct Photons

Experimental techniques for measuring direct photons are focused on reducing the large contribution from meson decays. Two standard techniques in p+p collisions include *invariant mass*

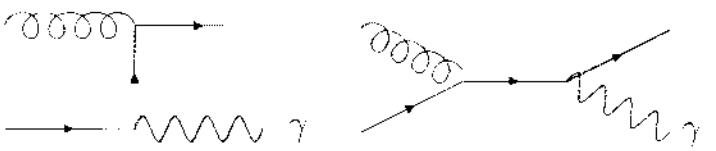

(a) The leading order gluon Compton scattering QCD diagrams of prompt photon production

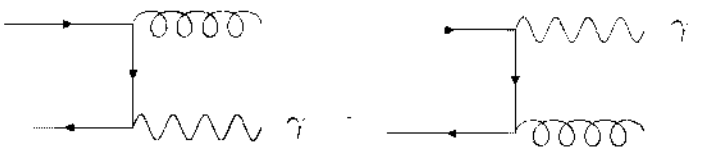

(b) The leading order quark annihilation diagrams

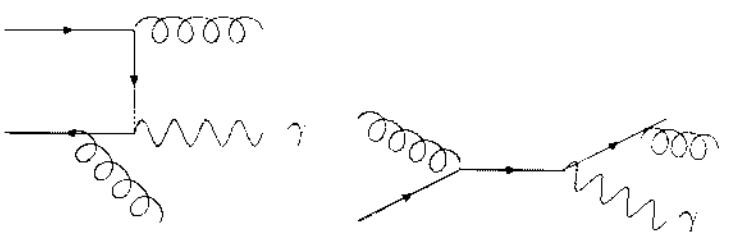

(c) Two examples of next to-leading order diagrams

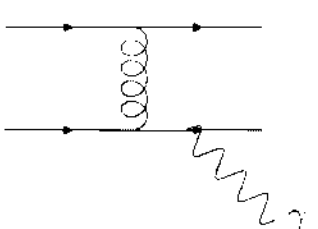

(d) A pQCD calculable component of photon bremsstrahlung

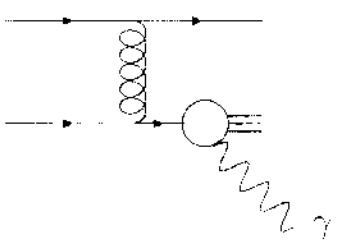

(e) A fragmentation photon produced in photon bremsstrahlung

Figure 2.7: Feynman diagrams contributing to leading order (LO) and next-to-leading-order (NLO) pQCD photon production calculations.

analysis, where pairs of photons having invariant mass close to the π^0or η mass are rejected, and *isolation cuts*, where the photon candidates are required to have no other high-p_T particles around them. The high multiplicity in high-energy nuclear collisions limits the application of these techniques.

Isolation cuts exploit the fact that photons produced in jet fragmentation tend to be accompanied by other jet fragments. A cone of a certain radius is formed around the direct photon candidate and events which have either another particle in the cone or the energy summed within the cone above a threshold energy are rejected. This particular method of isolation cuts is not suitable for a theoretical treatment, because of difficulties with infrared singularities (divergences in the calculations when very low momentum gluon radiation is included). An infrared-safe prescription for an isolation cut has been proposed by Frixione [66].

To date, two heavy-ion experiments (WA98 and PHENIX) have reported direct photon results, using very similar experimental techniques. The technique used by PHENIX, at RHIC, will now be discussed. The inclusive photon spectra were measured and the contribution

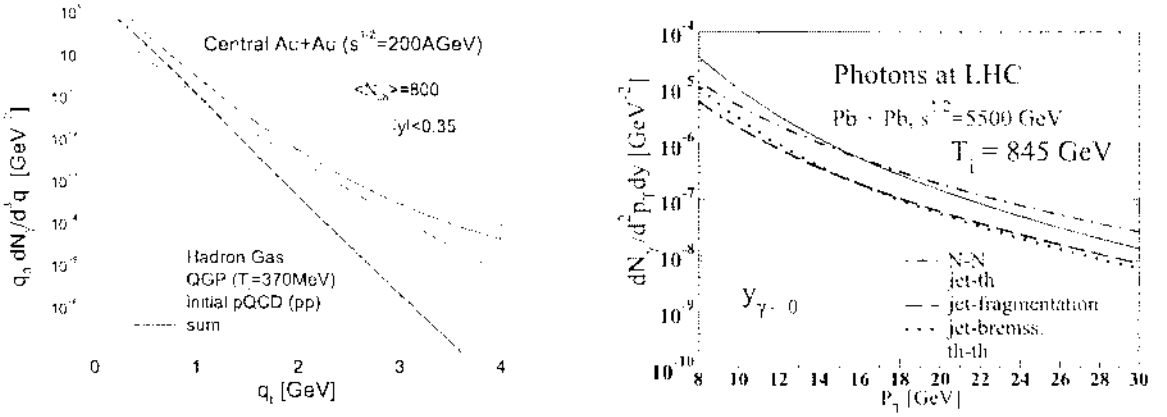

(a) Predicted thermal and NLO pQCD photon spectra for RHIC comparing photons from the QGP (red) and the HG (blue) from [62]

(b) Sources of high p_T photons in central Pb+Pb collisions at the LHC [63]

Figure 2.8: Predictions of the relative magnitude of photon sources.

from charged particle and neutron backgrounds was subtracted. An accurate measurement of the π^0 and η spectra was made and the expected decay photons calculated. The decay photon spectrum is subtracted from the inclusive photon spectrum to obtain the direct photon spectrum as follows:

$$\gamma_{direct} = \left(1 - \frac{\left(\frac{\gamma_{decay}}{\pi^0}\right)_{calc}}{\left(\frac{\gamma_{incl}}{\pi^0}\right)_{meas}}\right) \times \gamma_{incl} \tag{2.2}$$

The double ratio is used because correlated uncertainties in the γ and π^0 measurement cancel in $\left(\frac{\gamma_{incl}}{\pi^0}\right)_{meas}$. The ratio $\left(\frac{\gamma_{decay}}{\pi^0}\right)_{calc}$ was calculated from Monte Carlo simulations.

At SPS, WA98 reported the first direct photon measurement (Figure 2.9(a)) in 158 GeV Pb+Pb collisions in 2000 [67]. They found a 20% enhancement in the $\gamma_{meas}/\gamma_{bkg}$ ratio in central collisions (Figure 2.9(a) (bottom)) with no significant signal in peripheral collisions (Figure 2.9(a) (top)). Their results can be explained by both HG and QGP interpretations.

The first measurement of direct photons at RHIC was reported by PHENIX at Quark Matter 2004 [69] and agrees within errors with pQCD scaled by the number of binary collisions. The latest results show that the direct photon results agree with NLO pQCD calculations over all centralities (Figure 2.9(b)), a somewhat surprising result given the many different photon sources.

2.5.2 High-p_T photon measurements at the LHC

The abundant production of photons at the LHC will allow the measurement of photon correlations as well as the photon spectrum. High-p_T photon studies capitalise on the rapid increase of the γ/π^0 ratio with particle energy.

The energy loss of a high-p_T parton can be studied using photon-hadron or photon-photon correlations, using the photons produced in the γ-jet process. In γ-jet production, the photon and the recoil jet have identical initial energy, therefore the order of magnitude more accurate photon energy resolution (cf. Section 6.1 and [52]) can be used to study the changes to jet fragmentation functions due to the medium [54]. This naive picture is complicated by the fact that photons are also produced through bremsstrahlung, which reduces the correlation

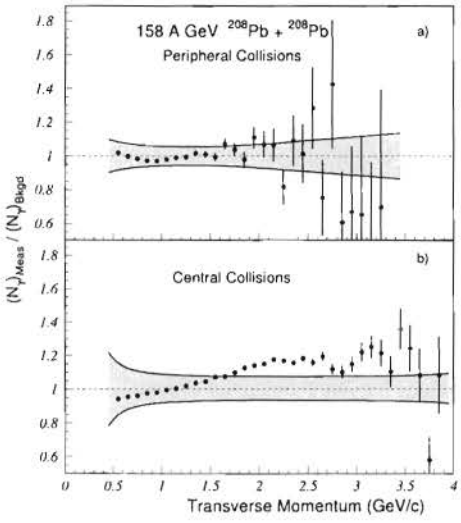

(a) The $\gamma_{meas}/\gamma_{bkg}$ ratio as a function of the transverse momentum for peripheral (a) and central(b) 158 A GeV Pb+Pb collisions as measured by the WA98 Collaboration [67].

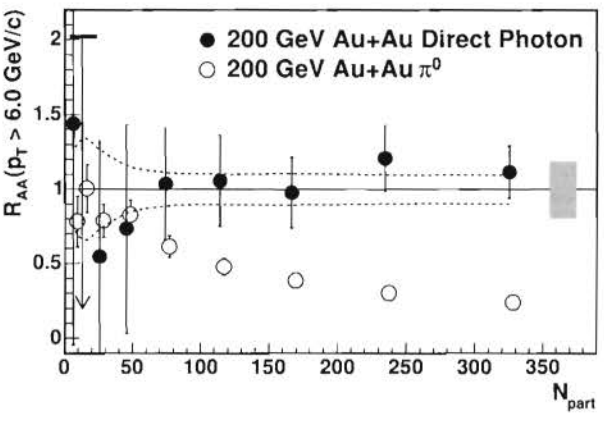

(b) Ratio of Au+Au yield normalised by the number of binary nucleon collisions as a function of centrality for direct photons (closed circles) and π^0 s (open circles) as measured by the PHENIX collaboration [68]. The p+p yield is taken to be a NLO pQCD prediction. The dashed lines indicate the range of theoretical predictions.

Figure 2.9: Direct photon results from WA98 and PHENIX.

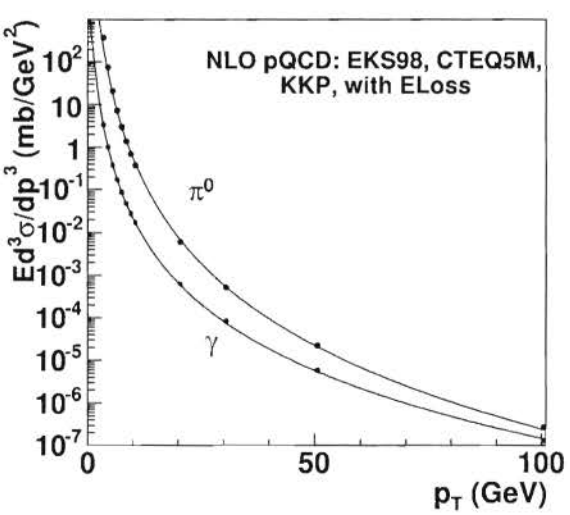

(a) NLO pQCD predictions (circles) of the invariant cross-section for direct photons and π^0s at 5.5 TeV [70, 71] with the power law fits used in Section 6.3

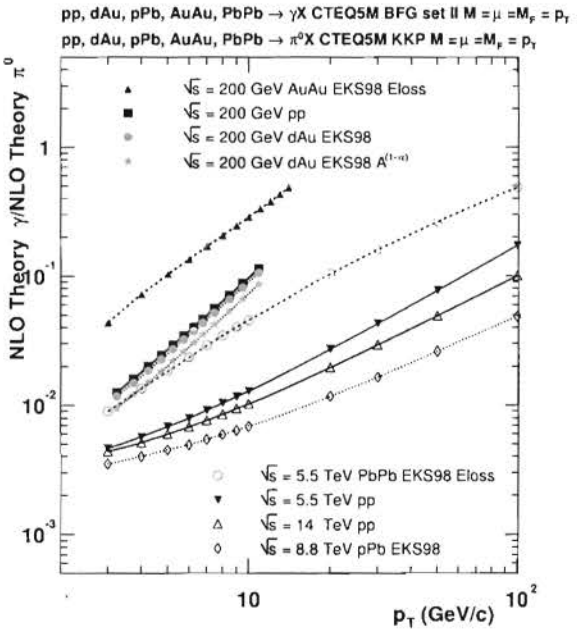

(b) NLO pQCD predictions for the ratio γ_{prompt}/π^0 in p+p, p+Pb and Pb+Pb collisions at 200 GeV and 5.5 TeV from [70]. The blue circles were used in Section 6.3 to scale the photon and π^0 simulations.

Figure 2.10: NLO pQCD predictions for direct photons and neutral pions.

between the photon and jet momenta. Jet pair production is dominated by gluons, unlike γ-jets, therefore γ-jet production will provide a means to measure quark energy loss.

It has been shown that a simple method using $\gamma - \pi^0$ and $\gamma - \gamma$ correlations [72] can be used to measure parton fragmentation functions. These correlations can be studied at lower transverse momentum than γ-jets where jet identification is difficult, and have shown to be effective even with a large contribution from bremsstrahlung photons.

The prompt photon and π^0 invariant cross-sections at the LHC from a NLO pQCD calculation [70], including an assumption for π^0 suppression from jet energy loss, are compared in Figure 2.10(a). These calculations include nuclear shadowing (EKS98) and use the CTEQ5M structure function and KKP fragmentation. The ratio of prompt photons to π^0s is compared in Figure 2.10(b), with the predictions for the LHC with energy loss (blue open circles) an order of magnitude below that at RHIC (red triangles). This makes it clear that it will be very important to distinguish between photons and neutral pions, which will be the topic of this thesis.

Chapter 3

Experimental Apparatus

The results that will be presented here were obtained from simulations of the Electromagnetic Calorimeter (EMCal) of ALICE, one of the future LHC experiments. This chapter provides a brief overview of the LHC and its experiments. A more detailed description is provided of the ALICE detector components, focused on the EMCal. The mechanisms of showering in calorimeters are discussed and different methods of $\gamma - \pi^0$ discrimination are introduced in the context of the EMCal.

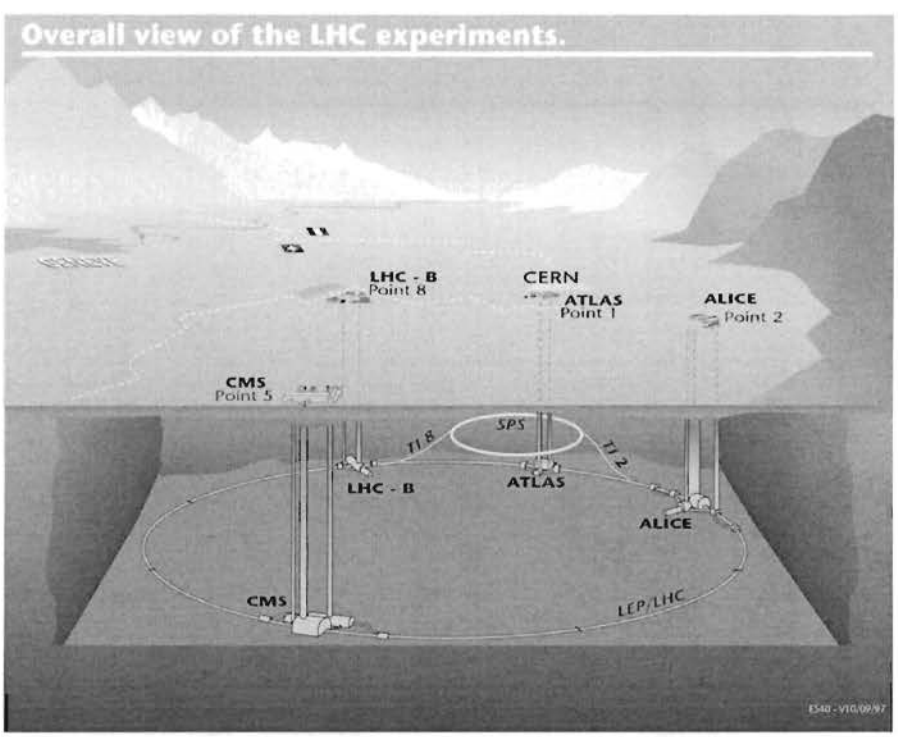

Figure 3.1: The location of the LHC and its experiments [73]. The ALICE experiment is located at Point 2, in France, on the right.

3.1 The Large Hadron Collider

The LHC is currently under construction in the existing Large Electron Positron Collider (LEP) tunnel at the European Organization for Nuclear Research (CERN) near Geneva (see Figure 3.1). The LHC will have a circumference of approximately 27 km and be located 100 m underground. Protons will be collided with an energy of 14 TeV (in the centre of mass frame) and lead ions with an energy of 5.5 TeV per nucleon (1148 TeV per Pb nucleus). The LHC will

be the highest energy accelerator in the world and is scheduled to begin proton-proton collisions in 2007 with the first heavy-ion collisions in 2008. The ions are accelerated in energy steps

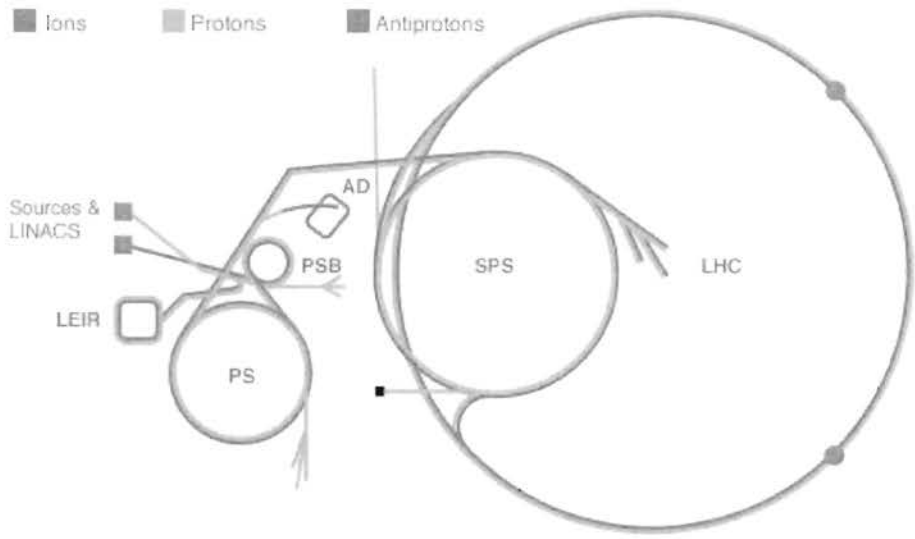

Figure 3.2: The injection scheme at the LHC for protons (orange), antiprotons (red) and ions (blue) at the LHC [73]. See text for discussion.

(see Figure 3.2), reusing the accelerators from earlier CERN experiments, in the following sequence:

- Accelerated to an energy of 4.5 MeV in the linear accelerator (LINAC)
- Accelerated to 26 GeV in the Proton Synchrotron (PS)
- Accelerated to 450 GeV in the Super Proton Synchrotron (SPS)
- Injected into the LHC and accelerated to 2.75 TeV

The LHC has separate magnetic channels for the two beams within a single twin bore superconducting magnet, which produces a magnetic field of 8.36 T [74]. The design peak luminosity for lead ions is $10^{27}\ \mathrm{s}^{-1}\mathrm{cm}^{-2}$ [74] and a summary of some of the significant LHC design parameters are provided in Table 3.1. The ion beam will have a bunch crossing time of 100ns, four times as long as that in p+p, to reduce event pile-up in the ALICE detectors.

There will be five experiments at the LHC. A Toroidal LHC ApparatuS (ATLAS) and the Compact Muon Solenoid (CMS) are the two large proton-proton experiments intended to discover the Higgs boson and physics beyond the Standard Model. LHCb, a smaller experiment, will explore CP violation in the B_s meson sector. TOTEM is dedicated to the measurement of total cross section, elastic scattering and diffractive processes using Roman pots, located within the CMS cavern. ALICE is the dedicated heavy-ion detector and, as the focus of this thesis, its various components will be discussed in more detail in the next section.

3.2 A Large Ion Collider Experiment

ALICE, as the dedicated heavy-ion experiment at the LHC, is optimised to analyse Pb+Pb collisions at $\sqrt{s} = 5.5\ \mathrm{TeV}$ (25 times more energy than today's most advanced accelerators). ALICE is a 14m long cylindrically shaped detector with a diameter of 10m. It will measure

Parameter		*p+p*	*Pb+Pb*
Centre of mass energy	TeV	14	5.5
Injection energy	GeV	450	180
Luminosity	$\mathrm{cm}^{-2}\mathrm{s}^{-1}$	2.3×10^{34}	1.8×10^{27}
Bunch spacing	ns	25	99.8
Particles per bunch		1.67×10^{11}	7.0×10^{7}
RMS bunch length	cm	7.55	7.94
Number of bunches		2808	592
Luminosity lifetime	h	10	10
Dipole field	T	8.33	

Table 3.1: Current ultimate LHC beam parameters for p+p and Pb+Pb collisions at top energies [74]

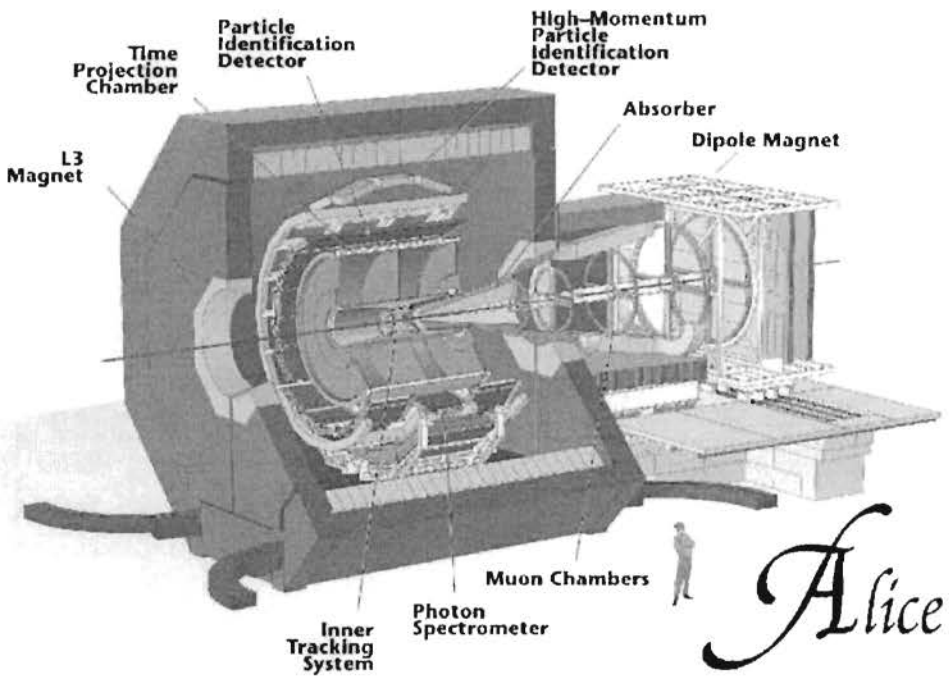

Figure 3.3: An artist's impression of the ALICE Detector with subdetectors labelled. The EMCal is not shown.

hadrons, leptons and photons over a large phase space to study nuclear matter under extreme conditions and possibly the Quark-Gluon Plasma (QGP).

One of the main challenges in Pb+Pb collisions at the LHC is the large predicted particle multiplicity and the ALICE experiment has been specifically designed for such an environment. The ALICE detectors are shown in Figure 3.3, with a set of central barrel detectors inside the magnet from the L3 experiment and a muon spectrometer at forward rapidity.

The **Inner Tracking System (ITS)** is the detector closest to the interaction point. It consists of six cylindrical layers of silicon wafer covering the central rapidity region and will be used for tracking and vertex reconstruction to identify weak decays.

The **Time Projection Chamber (TPC)** continues tracking once the particles are outside the ITS. The TPC is the main tracking detector of the central barrel and covers a pseudorapidity range of $|\eta| < 0.9$. The TPC, together with the **Transition Radiation Detector (TRD)** and the **Time Of Flight (TOF)**, provides charged particle momentum measurements from

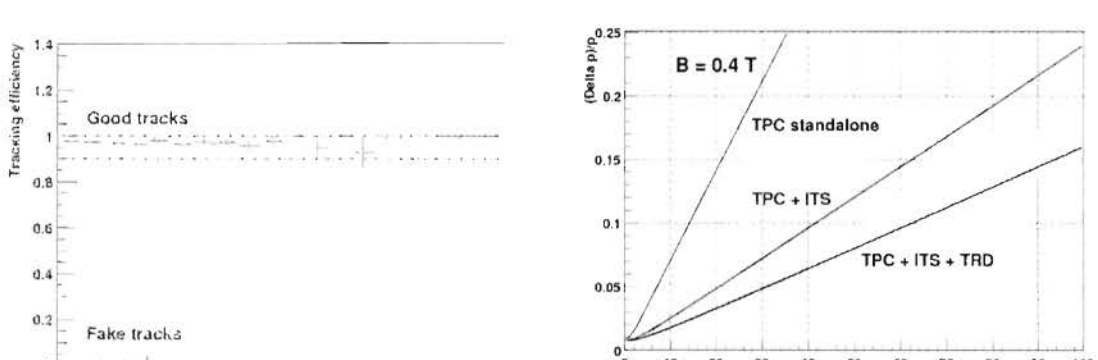

Figure 3.4: The charged particle tracking efficiency (left) and momentum resolution (right) for charged particles obtained from simulations using the ALICE detectors (left) [75].

100 MeV/c to 100 GeV/c with excellent resolution and efficiency [75] (Figure 3.4).

The TOF will identify low-momentum particle. The **High-Momentum Particle Identification Detector (HMPID)** using ring-imaging Cherenkov technology to identify higher-momentum particles. Beyond the momentum coverage of the HMPID, the TPC can provide charged particle identification by measuring the energy loss.

The TRD is optimised for electron measurements from charmonium decays. The **Dimuon Arm** lies outside the central barrel and will measure the production of heavy vector mesons including the J/Ψ and the Υ family through the muonic decay channel.

The **Photon Spectrometer (PHOS)** is optimised for photon detection to measure γ-jets and thermal photons. PHOS is a finely segmented, small area lead-glass calorimeter ($|\eta| < 0.12$, $\Delta\phi = 140\,\mathrm{deg}$) with an additional charged particle veto (CPV) to reject energy deposited by charged particles. There is significant complementarity between the EMCal and PHOS and this will be discussed further in the following section where the properties of the EMCal are introduced.

3.3 The Electromagnetic Calorimeter

The Electromagnetic Calorimeter (EMCal), proposed by the ALICE-USA collaboration, extends the limited calorimetric coverage of PHOS, and allows the detection and characterisation of high-p_T particles coming from the fragmentation of hard partons. It will enhance the jet reconstruction capabilities of ALICE by measuring the energy of the neutral particles in jets, providing an efficient trigger on high-energy particles and extending the transverse momentum coverage of rare high-p_T processes such as γ-jets. The EMCal is a sampling calorimeter with

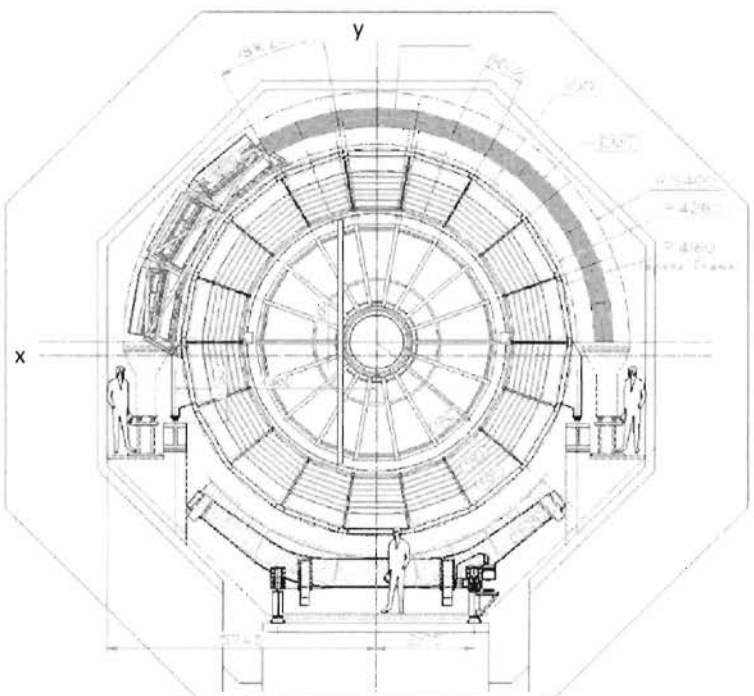

Figure 3.5: An engineering drawing of cross-section through the ALICE detector. The EMCal is indicated in orange.

alternating layers of lead and scintillator covering 1.4 units of pseudorapidity (η) and 110^o in azimuth (ϕ). In heavy-ion collisions at LHC energies, the rate for high-p_T processes will be large so that full azimuthal coverage will not be necessary. There is currently an ongoing effort to determine the optimum number of towers and segmentation but, it will be assumed in this thesis that there are 114 towers in η and 168 in ϕ, yielding a total of 19152 towers [1]. This translates into a 5.29 by 5.44 cm tower size at the front face of the EMCal. These towers are projective [2] and have an angular width of $\sim$0.012 radians, about four times larger than PHOS towers.

The EMCal will be built from 12 super modules each covering 0.7 radians in η and 20^o in ϕ and weighing about 9.6 tons. These super modules segmented into four in the ϕ direction (Figure 3.6) to make 48 modules. The modules consist of 57 towers in η and seven towers in ϕ.

Figure 3.7 shows the layers of each tower. The layers of lead and scintillator are each 5 mm thick. Table 3.2 compare the radiation lengths of the different tower materials. The

[1] The tower segmentation in the current design is 96 by 144, a total of 13824

[2] A projective tower is oriented with the length lying along a radial line from the interaction point

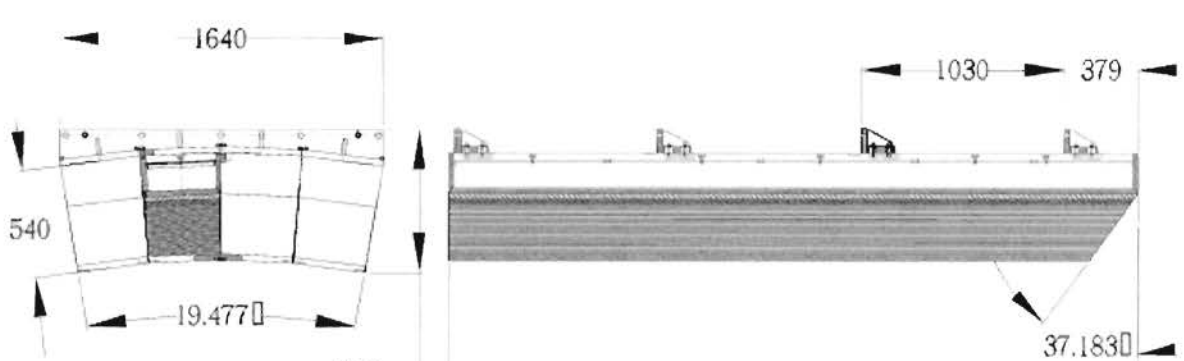

Figure 3.6: An ALICE EMCal super-module (dimensions in mm) with ϕ in the horizontal direction (left). A individual module with η in the horizontal direction (right).

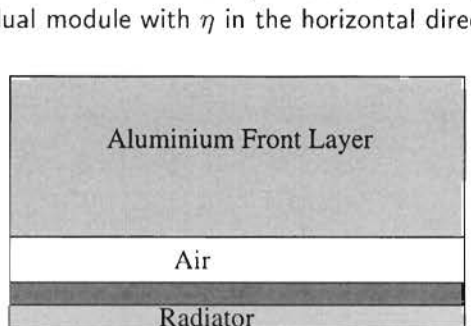

Figure 3.7: Schematic diagram of an EMCal tower. The material with the edge closest to the interaction point is at the top. Each EMCal tower contains 24 layers of lead and 25 layers of scintillator. Note that the towers are trapezoidal (not shown here) so that they are projective.

Material	*Radiation length*
Polystyrene	42.9 cm
Aluminium	8.9 cm
Lead	0.56 cm

Table 3.2: The radiation lengths for the materials in the calorimeter [76]

radiation length is defined as the distance over which the electron loses $1 - e^{-1}$ (63%) of its energy through bremsstrahlung and sets the length scale of the electromagnetic shower (see Section 3.3.1 for further discussion). The current design of the calorimeter has approximately 23 radiation lengths, sufficient to contain the showers from photons with energies up to 100 GeV. Simulations have shown that photons with energy above 100 GeV do not deposit all their energy, and punch through to the far side of the calorimeter (Figure 3.8). This results in a non-linear calorimeter response and increased fluctuations in the deposited energy, which degrades the energy resolution.

PHOS and the EMCal are both electromagnetic calorimeters and are compared in Table 3.3. Although PHOS has a smaller granularity and superior energy resolution, the EMCal has seven times greater acceptance, allowing the EMCal to measure rare processes to higher transverse momentum.

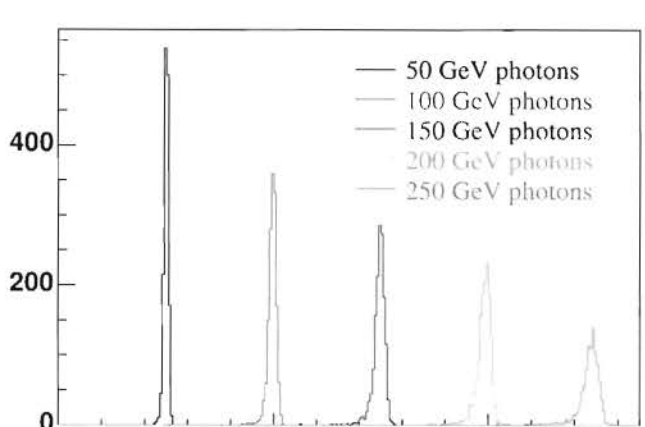

Figure 3.8: The energy deposited in the calorimeter by photons as a function of increasing energy. The photons with energies above 100 GeV have non-Gaussian energy distributions, because they "punch-through" the back of the EMCal.

Quantity	*EMCal*	*PHOS*
η coverage	$\|\eta\| < 0.7$	$\|\eta\| < 0.13$
ϕ coverage	$\Delta\phi = 120^o$	$\Delta\phi = 140^o$
Tower size (radians)	0.012	0.004
Energy resolution	$\frac{\Delta E}{E} = \frac{0.07}{E} \oplus \frac{0.2}{\sqrt{E}} \oplus 0.04$	$\frac{\Delta E}{E} = \frac{0.013}{E} \oplus \frac{0.036}{\sqrt{E}} \oplus 0.0112$

Table 3.3: Comparison of PHOS and the EMCal

3.3.1 Particle Showers in Calorimeters

A particle traversing matter interacts and loses energy thereby exciting the medium. These interactions can be one of the strong, electromagnetic or the weak interactions depending on the particle type. This section discusses the different energy loss processes as well as the development of showers in the context of the EMCal.

3.3.1.1 Electromagnetic Showers

A photon loses energy through four electromagnetic processes: the photoelectric effect, coherent (Rayleigh) scattering, incoherent (Compton) scattering and electron-positron pair production. The photons studied in this thesis are in the energy range where pair production is the dominant process. Pair production occurs only within the field of a charge particle. The electron and positron lose energy by ionising the medium and through bremsstrahlung until the electron is absorbed and the positron annihilates with an electron. Since, a photon converts into an electron-positron pair, the showers from photons and electrons are very similar. A significant difference, though, is that the electron immediately begins losing energy in the detector, while the photon travels a distance into the material before converting. This distance is known as the mean free path and is related to the radiation length.

Electromagnetic shower development is primarily determined by the electron density of the medium so that showers can be characterised by material independent parameters. The shower dimensions are described by the *radiation length* (X_0) and the *Molière radius* (ρ_M). The mean free path of a high-energy photon is approximately $\frac{9}{7}X_0$ [77], where X_0 is the radiation length. As electromagnetic showers develop longitudinally the rate of energy deposition increases as the number of particles in the shower increases, through pair conversion, until the average

energy of the shower particles falls below the critical energy, after which the shower photons are more likely to produce one electron through Compton or photoelectric interactions. This is known as the *shower maximum* and the distance to the shower maximum increases with particle energy.

The Molière radius is a measure of the transverse development of a shower and 95% of the shower energy is deposited on average within the Molière radius. Shower broadening is caused by particles which have been produced through multiple scattering, Compton and the photoelectric effect moving away from the shower axis. Multiple scattering occurs more often during in the early phases of shower development while Compton scattering and the photoelectric effect are dominant beyond the shower maximum.

3.3.1.2 Hadronic Showers

Hadronic showers are more complicated than electromagnetic ones, because the strong interaction causes many processes on both the particle and nuclear level. Charged hadrons lose energy through a combination of electromagnetic and strong processes, while neutral hadrons, such as neutrons, can only lose energy through nuclear reactions. Ionisation is the dominant method of electromagnetic energy loss for charged particles other than electrons. The median energy deposited by these particles is independent of energy but there is a distribution up to the original value. The π^0, decays electromagnetically into two photons almost immediately, hence its showers will be electromagnetic, despite the fact that it is a hadron.

Hadronic shower length is governed by the nuclear interaction length, λ_{int}: the average distance a high-energy hadron has to travel in a material before a nuclear interaction occurs. The interaction length depends on the number of protons in the material as well as the size of the particle interacting. The absorption of hadronic showers requires considerably more material than for the electromagnetic showers of the same energy. Hadronic showers are considerably broader than electromagnetic showers and consist of two parts: a narrow electromagnetic core and an exponentially decreasing hadronic halo. Fluctuations in hadronic showers are also larger, due to the many competing processes. For further discussion of both electromagnetic and hadronic showers, see [77].

3.3.2 γ-π^0 discrimination in the EMCal

When a π^0 decays into two photons, the angle between the momentum vectors of the two photons, is determined by the energy of the π^0 and the asymmetry of the decay. The asymmetry of the decay is a measure of how π^0 energy is shared between the two photons. This opening angle decreases with increasing energy (Figure 3.9) and, in terms of number of towers, sets the scale of the resulting shower and hence the analysis techniques to be used for γ - π^0 discrimination.

At low energies the decay photons are well separated, forming two separate clusters of energy, and can be reconstructed using standard techniques of invariant mass analysis (see Section 6.2.2). At higher energies, the energy clusters of the photons overlap and the photons cannot be separately reconstructed, but the shape of the shower from the two photons is asymmetrical and very different from that of a single photon. In this region shower shape analysis can be used, where the shapes of the showers are fitted to determine whether they are photons or not (see Section 6.2.1). At even higher energies the two photons are so close together that their shower shape is indistinguishable from that of a single photon. In this region one has to resort to using isolation cuts, which reject photons if there are other particles within a cone of a certain radius formed around the photon.

Note that the regions in energy, in which these different analyses are used, depend strongly on the granularity of the detector. In the EMCal invariant mass works well until approximately

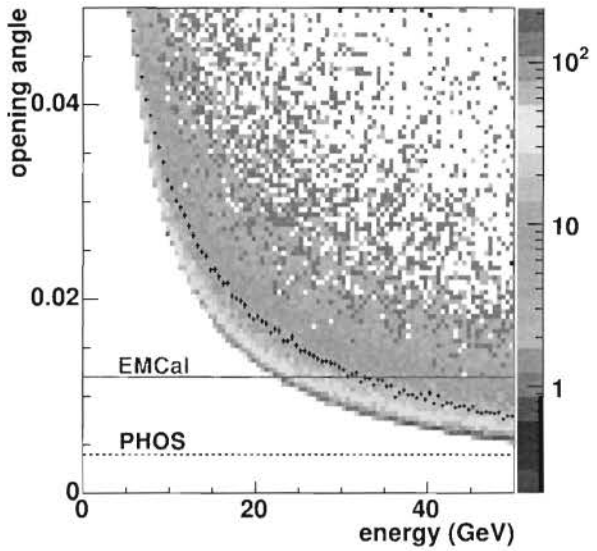

Figure 3.9: The opening angle of the decay photons from π^0 s in the LAB reference frame as a function of the π^0 energy. The size of one EMCal tower (red line) and one PHOS tower (black dashed line). The mean π^0 opening angle is superimposed in black.

12 GeV and shower shape analysis until approximately 50 GeV. PHOS, in contrast, has towers four time smaller than the EMCal, which means that shower shape analysis can be used to significantly greater energies (compare the black dashed line in Figure 3.9).

This thesis will provide an analysis of photon and π^0 showers using Monte Carlo simulations of the EMCal. Invariant mass reconstruction will be demonstrated, but the focus will be on the results that can be obtained using shower shape analysis. Isolation cuts were not investigated because the EMCal acceptance is not suitable for their use.

Chapter 4

Simulation and Reconstruction

This section details software used in and developed for this thesis. The simulations used Monte Carlo event generators, followed by a ROOT-based program to approximate the EMCal response. A method of characterising particle showers is introduced, which will later be used for $\gamma - \pi^0$ discrimination.

4.1 The AliRoot Framework

All simulations and reconstruction algorithms were run within the AliRoot framework: a software program based on ROOT [78]. ROOT is a software package widely used in experimental high-energy physics, which provides a set of object oriented classes to manage and analyse large amounts of data efficiently. Within AliRoot, collisions are simulated using the Monte Carlo event generators, PYTHIA [79] (for p+p collisions) and HIJING [80] (for Pb+Pb collisions). The program GEANT3 [81] tracks the interactions and energy loss of particles passing through the detectors and simulates the detector response.

The software for all the ALICE detectors, including the EMCal, follows the same simulation steps as illustrated in Figure 4.1. GEANT calculates the energy deposited by a particle passing through the detector and the further simulation steps are used to modify this to estimate the signal produced by the real detectors using known physics processes.

4.1.1 Coordinate Systems

The ALICE experiment uses a right-handed orthogonal Cartesian system with the interaction point at the origin of the coordinate system [82]. The axes and angles are defined as follows:

- The **x axis** lies perpendicular to the beam direction, parallel to the ground and positive x points towards the accelerator center.
- The **y axis** is perpendicular to the x axis and the beam direction with positive y pointing upwards.
- The **z axis** is parallel to the beam direction with positive z towards the town of Bellegarde, lying to the east. The muon arm lies at negative z.
- The **azimuthal angle** ϕ increases counter-clockwise from x ($\phi = 0$) to y ($\phi = \frac{\pi}{2}$) with the observer standing at positive z and looking through the interaction point towards Gex, which lies to the west.
- The **polar angle** θ increases from the positive z axis($\theta = 0$) to the x-y plane ($\theta = \frac{\pi}{2}$) to negative z axis ($\theta = \pi$).

The EMCal is a fraction of a cylinder with is axis lying along the beam line. As such, the natural coordinate system to use is the azimuthal angle, ϕ and the pseudorapidity, η. The pseudorapidity is dimensionless and ϕ will be expressed in radians for consistency.

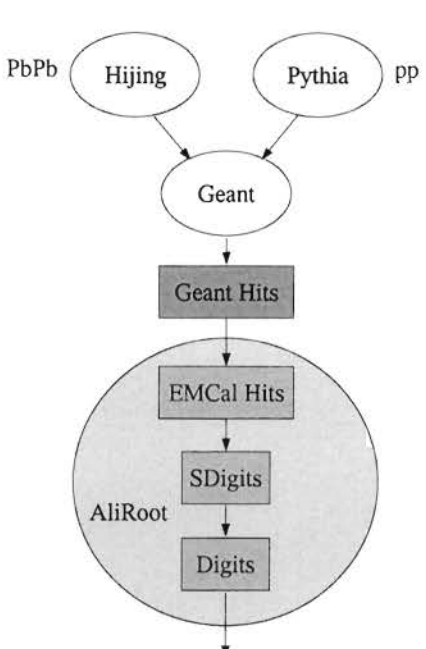

Figure 4.1: The steps of the simulation process for the EMCal within the AliRoot framework. PYTHIA (HIJING) is used to simulate the p+p (Pb+Pb) events. The simulated particles are tracked by GEANT, which records their energy loss in the detector material. One GEANT Hit is produced each time a particle interacts with matter and loses energy. The GEANT Hits are summed together in each EMCal tower, so that there is one EMCal Hit per particle per tower. The SDigits are constructed by summing the energies from different particles in each tower. The Digits consist of the SDigits convoluted with a parameterisation of the detector response.

4.2 Event Generation

This section outlines the different simulations in this thesis and highlights features of the Monte Carlo generators used. The photons and π^0s were embedded in Pb+Pb events (simulated with HIJING) to enrich the yield because they are rare high-p_T processes. The same Pb+Pb events were reused, because the embedded particles are distributed over the surface of the calorimeter. In this section, the simulations labelled "signal" refer to the single particles simulated and "background" to the simulations of the underlying event. In $\gamma - \pi^0$ discrimination, in contrast, the photons will be considered as the signal and the π^0s as the background.

4.2.1 Signal

Algorithms for the discrimination of photons and π^0s were developed from single particle shower shape profiles. There are two main background effects contributing: photon conversion in the material before the EMCal and particles from the underlying Pb+Pb event. Four different simulation cases were used to disentangle the contributions:

- The shower shape profile was obtained by simulating events containing single photons and π^0s with energies ranging from 0 to 100 GeV, with only the EMCal material.

- The conversion of photons in the material of the ALICE detectors was quantified by simulating single photon and π^0events over the same energy range with the addition of the other ALICE detectors.
- The effect of a high multiplicity background on single particle shower profiles was investigated by embedding these single particles without detectors in central Pb+Pb events, simulated using HIJING.
- The final results were obtained from the simulation of single particles with the detector material and embedded in central Pb+Pb events.

4.2.2 Background

The Heavy Ion Jet INteraction Generator (HIJING 1.36) [80] was used to simulate the background from the underlying heavy-ion event. HIJING simulates high-energy jets within heavy-ion collisions to test possible QGP signatures such as jet quenching and is based on PYTHIA with a Lund-type model for jet fragmentation [83]. Extrapolation from p+p to A+A collisions uses an optical Glauber model, with additional nuclear effects including nuclear shadowing of parton structure functions, parametrised jet energy loss and mini-jet production.

The number of charged particles per unit rapidity at mid-rapidity, $\frac{dN_{ch}}{dy}$, is the most important global observable in heavy-ion collisions. Predictions of $\frac{dN_{ch}}{dy}$ for central Pb+Pb events at LHC energy ranged from 2500 to 8000 before the first RHIC results, but measurements at RHIC for central collisions at 200 GeV yielded $\frac{dN_{ch}}{dy} \approx 650$ [84], a factor of two below most model predictions for RHIC. Linear extrapolation from RHIC data to the LHC predicts $\frac{dN_{ch}}{dy} = 2500$, but Figure 4.2 shows that HIJING predicts $\frac{dN_{ch}}{dy} = 5000$. This conservative background estimate was used in this thesis to ensure that the algorithms developed were robust in a high-multiplicity environment.

The number of particles produced increases with centrality as the collisions between the ions become closer to head-on collisions. The collision is classified by the distance between the centres of the two colliding nuclei, known as the *impact parameter*, b. As the impact parameter approaches zero, the collisions become more and more central. The background simulations in this thesis used the 5% most central HIJING collisions, which are henceforth referred to as central collisions. For lead nuclei, the 5% most central collisions have an impact parameter smaller than 3 fm.

The total energy deposited in the calorimeter in minimum bias HIJING events is shown in Figure 4.2. For 5% central collisions it ranges from 1.8 TeV to 2.4 TeV per event. This enormous background necessitates adaptations to the cluster finding algorithms used in p+p collisions such as the tower energy cut discussed in Section 5.4.

4.3 Detector Simulation

As shown in Figure 4.1 the simulation processes proceeds from event generation with the Monte Carlo programs, followed by digitisation. Digitisation uses three different intermediate data structures to store the energy deposited per particle per tower (*Hits*), the energy deposited per tower (*SDigits*) and the energy per tower convoluted with detector effects (*Digits*). Relevant details of these steps will now be discussed in the context of the EMCal.

4.3.1 Hits

There is one EMCal Hit per particle depositing energy in each tower. GEANT produces a hit every time a particle deposits energy in a layer of scintillator. All the hits from a particle in the

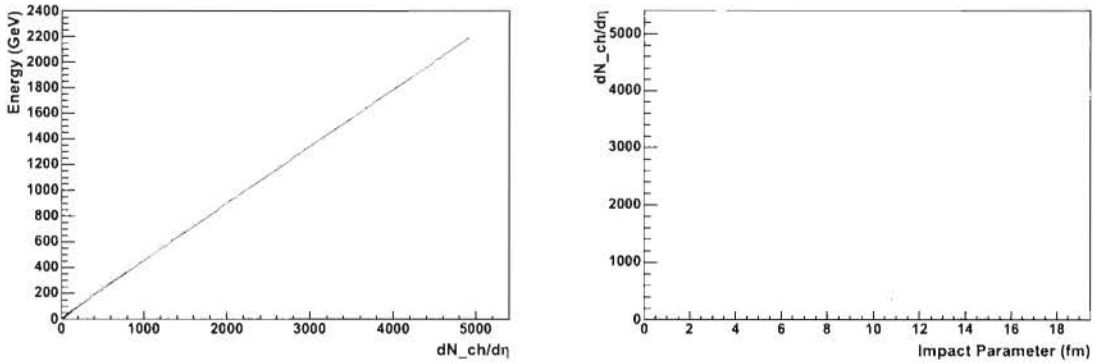

Figure 4.2: The measured calorimeter energy as a function of the number of charged particles per unit rapidity at mid-rapidity (left). This is in turn shown as a function of impact parameter.

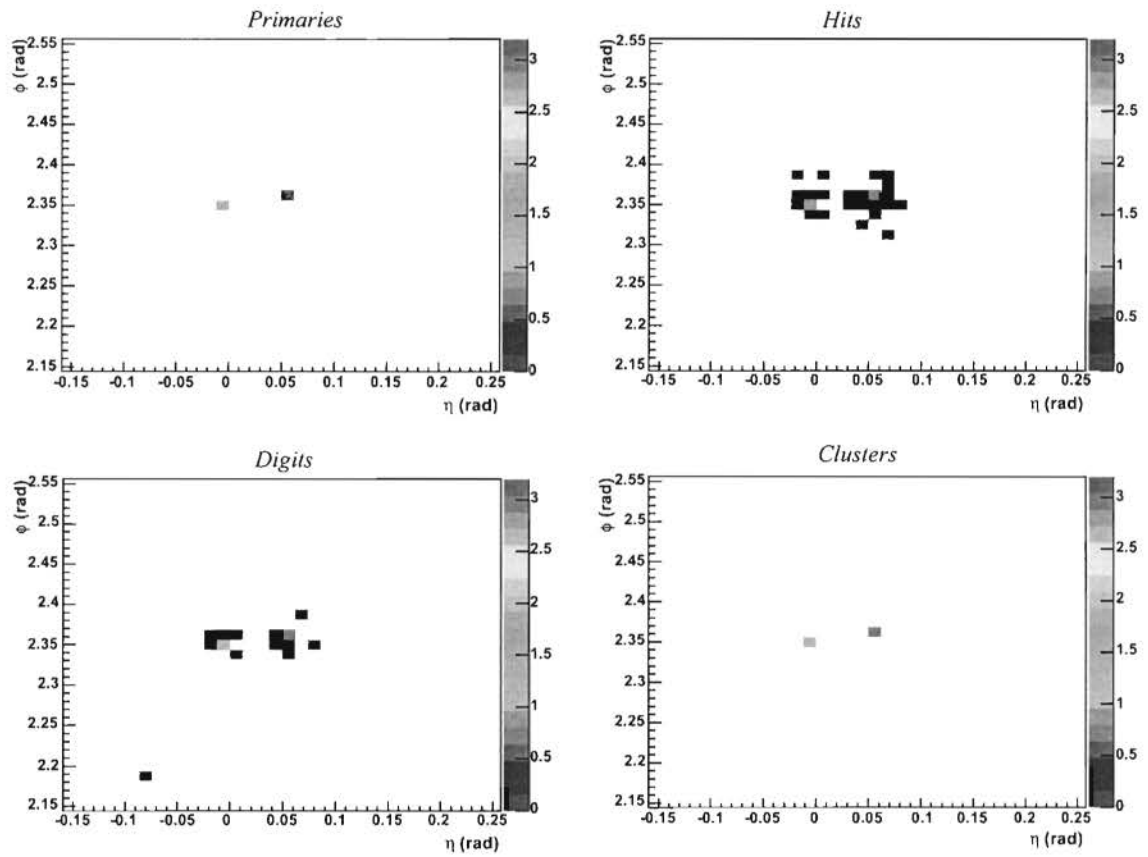

Figure 4.3: The energy of the decay photons of a 4.7 GeV π^0 at different stages of the simulation process. The Primaries (top left) show the energies of the two photons (taken directly from the Monte Carlo). The Hits (top right) show the energy deposited in the calorimeter material (output from GEANT). The energy of the SDigits (not shown) is qualitatively identical to the Hits for the EMCal. The Digits (bottom left) show the simulated detector read-out, including electronic noise. The Clusters (bottom right) are reconstructed using the clusterisation algorithm and should be compared to the Primaries.

different layers of a tower are added together to form the Hits. There is only one electronic read-out per tower for the EMCal, so this saves space while preserving the event information.

The time of this Hit is set to the time at which the particle first deposited energy, which generally occurs in the first layer of scintillator. This time refers to the arrival of the signal in the detector, not the timing information produced by the read-out electronics.

4.3.2 SDigits

SDigits (or summable digits) are made by summing together all the Hits in a tower, so that there is only one SDigit per tower. The arrival time of the resulting SDigit is set to the earliest time of the Hits. Note that this biases the SDigits energy-time distribution significantly when there are multiple particles depositing energy in the same tower as is often the case in heavy-ion collisions at LHC energies. For example, calculating the energy deposited within the first "30 ns" using the SDigits timing information, twice as much energy is found than if the Hit timing information is used. This is the reason that the Time Cut (see Section 5.4) is applied on the Hits and not the SDigits. If an SDigit has an energy below 100 MeV then the Monte Carlo particle originating the shower is not stored.

4.3.3 Digits

Digits are calculated by convoluting the SDigits with the detector response function including electronic noise and mean photon electron fluctuations. The signal has to be converted from an energy deposition (in GeV) to an amplitude that would be measured by the ADC:

$$Amp = \frac{E + ADC_{pedestal}}{ADC_{channelwidth}} \tag{4.1}$$

The ADC pedestal is the value read by the electronics in the absence of signal. It will be measured experimentally by taking pedestal runs. The electronics have 2^{16} channels and the energy range to be measured is from 0 to 200 GeV, resulting in an ADC channel width of 3 MeV. This channel width provides a lower bound on energy resolution, although this will be shown to be much small than the effects on energy resolution.

Fluctuations due to the number of electrons produced per photon are simulated by randomly sampling from a Poisson distribution. Electronic noise is simulated by selecting positive values from a Gaussian distribution with a mean of zero and $\sigma = 3$ MeV. A 9 MeV threshold was imposed to limit the number of towers containing only electronic noise being stored. The simulated electronic noise is added to any signal already found in a tower thereby smearing the deposited energy. After digitisation, the simulated data is in the same format as the real experimental data so that the same reconstruction software can be used in both cases.

4.4 Clusters

The first step in the reconstruction process is clusterisation. Clusterisation groups together energy in different towers to reconstruct all the energy deposited by a single particle. There are a number of possible algorithms and in this thesis two different ones were considered: the **patch algorithm** and the **n-search algorithm** .

4.4.1 Clustering Algorithms

Different clustering algorithms use different methods to find the digits are part of a single particle shower. The basic premise is that a particle tends to deposit its energy in nearby towers, although in the high multiplicity heavy-ion environment the showers from different particles tend to overlap.

4.4.1.1 The Patch Algorithm

The patch algorithm groups digits by placing a patch of fixed size centred on highest energy tower and adding all digits that lie within that patch to the cluster. Once digits are part of

a cluster, they are removed from the list of digits. This process is repeated with the next highest energy tower until there are no towers with energies above an energy threshold, called the clustering seed. Two different patch sizes were implemented: 9 and 25 towers.

4.4.1.2 The n-search Algorithm

The neighbour-search (henceforth n-search) algorithm starts with the highest energy tower and adds all its neighbouring digits to the cluster digit list. It then takes each digit in the cluster digit list in turn and adds all its neighbours. This continues until the digits in the cluster digit list have no further neighbours. There were two different definitions of *neighbours* implemented. The *n-search edge algorithm* defines neighbours as two towers with a common edge. The *n-search vertex algorithm* defines neighbours as two towers with either a common edge or a common vertex. Figure 4.4 illustrates the neighbours of the digit at the centre obtained using each of these definitions in turn.

In the high multiplicity of heavy-ion collisions at the LHC there are many overlapping showers and the clusters contain energy from many particles. A simple modification to the n-search algorithm was made by introducing a minimum tower energy cut in which towers containing energy below a certain threshold are ignored. The impact of this cut on shower shapes will be discussed in Section 6.2.1.

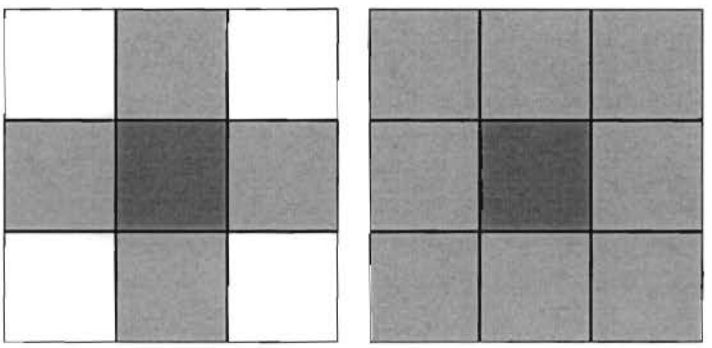

Figure 4.4: Neighbour definitions for the n-search and patch algorithms. On the left the neighbours of a tower are those towers, which share an edge, while on the right it is those towers that share at least a vertex.

4.4.1.3 Algorithm Comparison

The patch algorithm is quick to implement and run. It is little affected by the high multiplicity environment. It has no mechanism to deal with the increase in the number of digits with increasing photon energy, nor does it have a means of finding two overlapping clusters. This means that it could effectively be used for finding photons but would complicate the task of identifying merged π^0s.

The n-search algorithm is more sophisticated, does not assume a specific shower shape and handles the increase in the number of digits with particle energy. Contamination from shower overlap in the high multiplicity environment is reduced by the tower energy cut. This tower energy cut biases the algorithm in some non-intuitive ways. An obvious extension would be to include a routine to split clusters with multiple maxima using the shower profiles to apportion the energy between them. This is a far from trivial extension, but if it were implemented, it could mean that the minimum tower energy cut could be lowered significantly. Even without this modification, the n-search algorithm will be shown to be effective in particle reconstruction and $\gamma - \pi^0$ discrimination.

4.4.2 Shower characterisation

Once digits have been assigned to clusters, the next step is to calculate the position and energy of the cluster.

4.4.2.1 Energy and Position Calculation

The energy of a cluster is calculated by summing the energies of the digits in the cluster.

$$E = \sum c_i \tag{4.2}$$

The position of the incident particle is calculated as the centre of gravity of the digits weighted by their energies [85].

$$X = \frac{\sum x_i c_i}{E} \tag{4.3}$$

where x_i is the geometric centre of the ith tower. This method introduces systematic errors into the calculated position relative to the incident position, which increase with distance between the point of incidence and the module centre and reach a maximum as the point of incidence crosses the boundary between modules.

The energy deposition within a shower decreases logarithmically as a function of the distance from the shower centre. A linear weighting of the tower energy results in the calculation being dominated by a single high-energy tower, therefore alternative algorithms have been proposed.

One method takes the two towers on either side of the tower with maximum energy and calculates the position using the logarithm of the ratio of their energies. The other uses the logarithm of the ratio of the energies of the two towers with maximum energy. It was found that using a logarithmic weighting of energy improves the position resolution significantly [86] because shower energy decreases logarithmically with radius. The logarithmic weighting is used to calculate the tower position as follows:

$$X = \frac{\sum x_i w_i}{\sum w_i} \tag{4.4}$$

where

$$w_i = max[0, w_0 + \log \frac{c_i}{E}] \tag{4.5}$$

The dimensionless parameter w_0 plays two roles: it scales the contribution from the shower tails to the energy and provides a threshold for a tower to be included in the energy. See [86] for a full discussion. Because the value of w_0 is expected to be material independent for detectors with comparable tower sizes, a value of 4.5 [86] was used. The optimal value for the EMCal should ideally be obtained by balancing position resolution to contributions from shower shape fluctuations. Further corrections should account for the fact that the modules are not perpendicular to the interaction point [86, 87].

4.4.2.2 Cluster Shape

The differences between electromagnetic and hadronic showers are outlined in Section 3.3.1. Significant discriminatory power stems from the fact that hadronic showers are generally more disperse than electromagnetic ones. The size of a cluster is measured by calculated the lateral dispersion and has been used in the past for e/π discrimination.

The lateral dispersion is a measure of the size of the cluster. It is defined to be the mean squared deviation of the digits from the shower position. It is calculated in a similar way to the position, using logarithmic weighting as follows:

$$d = \frac{\sum w_i[(\eta_i - \eta)^2 + (\phi_i - \phi)^2]}{\sum w_i} \tag{4.6}$$

While the dispersion has proved useful in p+p collisions, it is sensitive to particles from the heavy-ion event depositing energy in towers neighbouring the perimeter. For this reason further shower shape parameters were explored.

The shape of a cluster assumed to be the intersection of a cone containing the shower with the front face of the EMCal. This surface can be expressed in terms of a covariance matrix of the variances in four directions. In EMCal coordinates, we calculate the variances from:

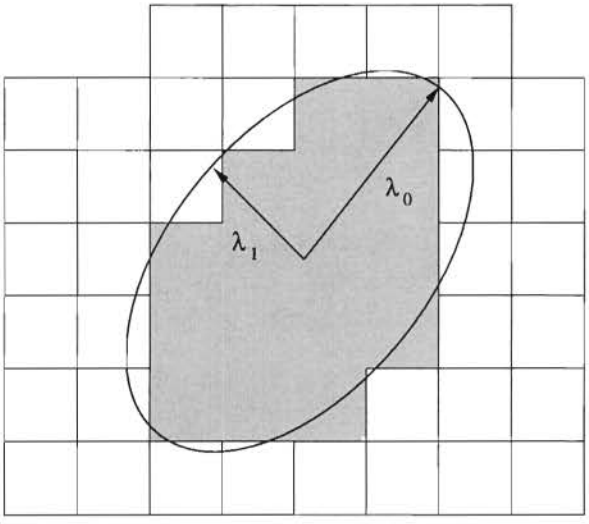

Figure 4.5: Example of digits in a cluster and the resulting shower profile

$$s_{\eta\eta} = \langle(\eta - \overline{\eta})^2\rangle \tag{4.7}$$

$$= \frac{\sum_{digits} w_i \eta_i^2}{\sum_{digits} w_i} - \left(\frac{\sum_{digits} w_i \eta_i}{\sum_{digits} w_i}\right)^2 \tag{4.8}$$

$$s_{\eta\phi} \equiv s_{\phi\eta} = \langle(\eta - \overline{\eta})(\phi - \overline{\phi})\rangle \tag{4.9}$$

$$= \frac{\sum_{digits} w_i \eta_i \phi_i}{\sum_{digits} w_i} - \frac{\sum_{digits} w_i \eta_i \sum_{digits} w_i \varphi_i}{(\sum_{digits} w_i)^2} \tag{4.10}$$

with an analogous definition for $s_{\phi\phi}$. These variances are the elements of shower shape tensor:

$$S = \begin{pmatrix} s_{\eta\eta} & s_{\eta\phi} \\ s_{\phi\eta} & s_{\phi\phi} \end{pmatrix} \tag{4.11}$$

The eigenvalues of this matrix are the lengths of the ellipse axes (λ_0 and λ_1 in Figure 4.5) sometimes called the first and second moments. The shower tensor is a symmetric 2x2 matrix so the eigenvalues are real and can be calculated from the following analytical formula:

$$\lambda_{0,1} = \frac{1}{2} s_\eta s_\phi \pm \frac{1}{2}\sqrt{(s_\eta - s_\phi)^2 + s_{\eta\phi}^2} \tag{4.12}$$

The sphericity, a measure of how much the cluster deviates from a circle, is obtained from λ_0 and λ_1:

$$S = \frac{|\lambda_0 - \lambda_1|}{\lambda_0 + \lambda_1} \tag{4.13}$$

It is possible to calculate the third and fourth cluster moments, but the second cluster moment was found to give sufficient discrimination capabilities. A further discussion of this method is given in [88]. Results from shower shape analysis for γ-π^0 discrimination in the EMCal will be presented and discussed in Section 6.3.

Chapter 5

Simulation Tuning

This chapter details preparatory studies to understand and reduce background effects caused by the detector material and the underlying Pb+Pb event. Photon conversions in the detector material were calculated; a sampling fraction was calculated to correct for energy loss in the lead; and Birks' law was added to improve the simulation of the hadronic response.

5.1 Sampling Fraction

The EMCal is a sampling calorimeter made of alternating layers of radiator (lead) and scintillator, but only the fraction of energy lost in the scintillator is measured. Therefore the scintillator layers are called *active material* and the lead layers are called *dead material*. A sampling fraction (the full energy divided by the measured energy) was calculated to correct for this using simulations of 10^6 mono-energetic (10 GeV) photons. Depending on the calorimeter material and design, sampling fractions can be both position and energy dependent. In the case of the EMCal, it is both position independent (Figure 5.1), except at the calorimeter edges, and energy independent (Figure 5.2), except for very low energy photons. Therefore a constant sampling fraction can be used with value of 13.1 ± 0.3, which was calculated from fits.

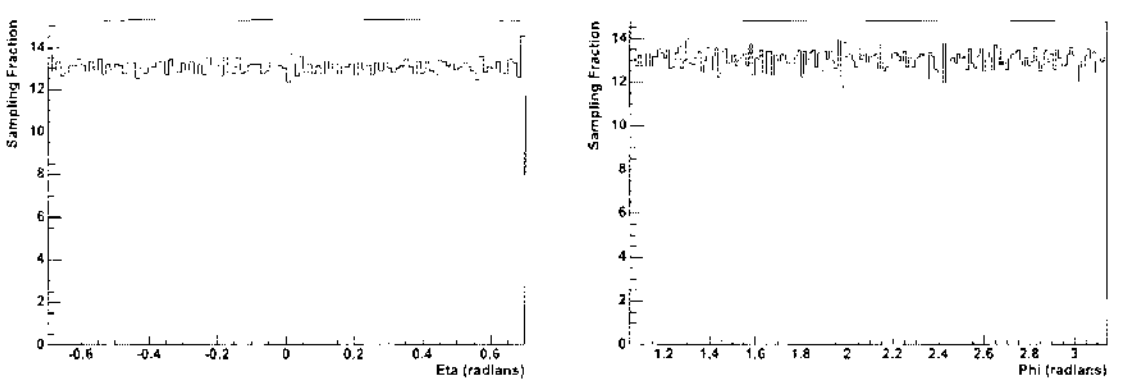

Figure 5.1: The Sampling Fraction as a function of η and ϕ. The simulation used 10 GeV photons incident at varying positions on the calorimeter. The sampling fraction is calculated from the incident/deposited energy.

5.2 Birks' Law

The light produced in the active calorimeter volumes is proportional to the energy lost through ionisation of charged particles. Organic scintillators (such as the EMCal) are known to be less efficient at converting high local energy loss to scintillation light. Birks' law [89, 90] corrects

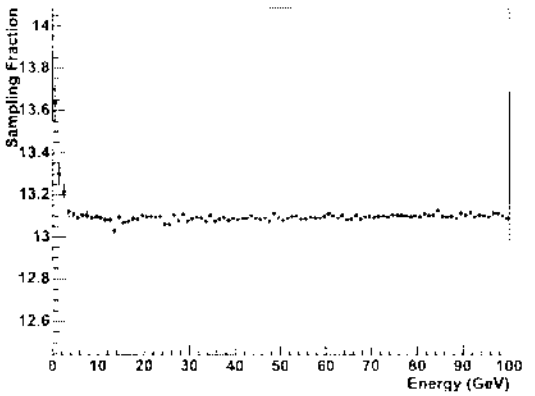

Figure 5.2: Sampling Fraction vs photon energy.

for this according to the following phenomenological formula:

$$\frac{dL}{dx} = \frac{S\frac{dE}{dx}}{1 + kB\frac{dE}{dx} + C(\frac{dE}{dx})^2} \tag{5.1}$$

where:

- $kB = \frac{kB_2}{\rho_{scint}}$
- $C = \frac{C_2}{\rho^2_{scint}}$

EMCal simulations take $kB = 12.6$ cmGeV^{-1} and $C = 0.0122$ cm^{2}GeV^{-2} calculated using the measured scintillator density ($\rho_{scint} = 1.032$ gcm^{-3}) and parameters from Craun [91]. The addition of Birks' law to EMCal simulations [92] decreased the calculations for the light yield from charged hadrons by approximately 10%.

5.3 Photon conversion

The front face of the EMCal is 464 cm from the interaction point, therefore photons pass through a large amount of material before reaching the EMCal. While passing through this material the photon can convert into electron-positron pairs, and begin showering before reaching the calorimeter. This broadens the showers observed in the calorimeter and they are more similar to those of π^0s. Figure 5.3 shows that 45% of photons convert before reaching the EMCal (red) and that this conversion fraction is independent of energy. These photon conversions occur most often in TRD (radial position of 294-368 cm), TOF and ITS as shown in Figure 5.4.

Photon conversions in the beam pipe and the ITS will be reconstructed in the TPC using a method similar to [93, 94], but these are only ~10% of the photons conversions (Table 5.1). Fortunately, many of the converted photons form narrow showers and still can be reconstructed in the EMCal.

5.4 Time Cut

Figure 4.2 showed that HIJING predicts that $\frac{dN_{ch}}{dy}$ in central collisions at the LHC will be 4000-5000 particles. Figure 5.5 (right) displays the energy measured by the calorimeter for

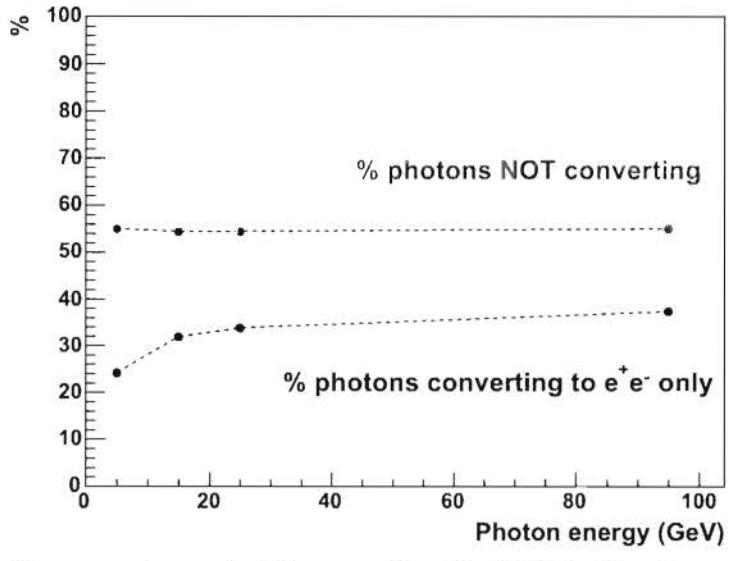

Figure 5.3: The percentage of photons reaching the EMCal without converting (red) with the material from all the ALICE detectors. The percentage of photons that convert to an electron-positron pair but do not shower further before the EMCal is shown below in black.

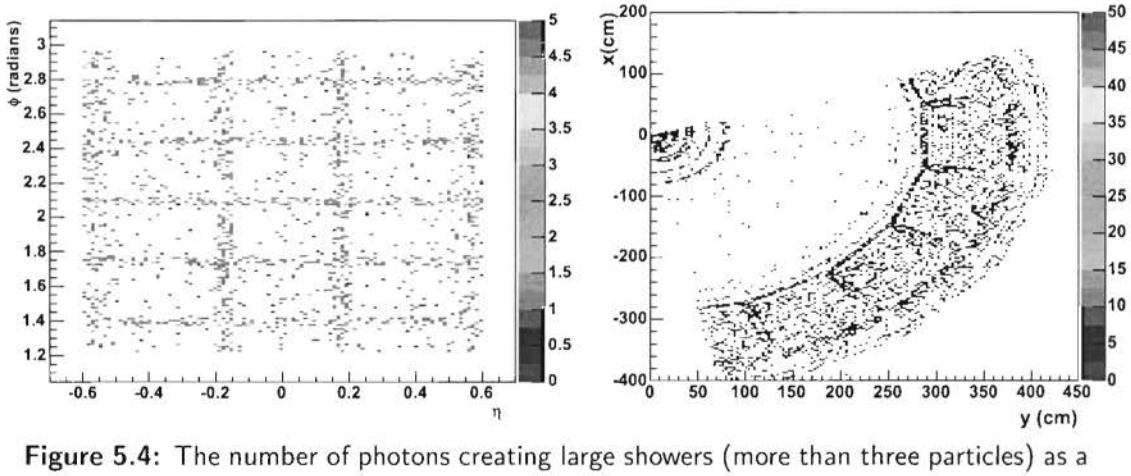

Figure 5.4: The number of photons creating large showers (more than three particles) as a function of the original photon η and ϕ (left). The regular pattern is due to the conversion in the structural supports of the TRD. The x and y positions at which the photons convert are shown on the right. The conversions at the top left are in the ITS and the conversions further out are in the TRD and TOF.

Detector	*% Photons Converting*
TRD	17.82%
TOF	9.14%
Beam pipe/ITS	5.75%

Table 5.1: The detectors with the largest percentage of photon conversions.

350 central HIJING events ($b < 3$ fm). This large amount of energy is caused both the high multiplicity in Pb+Pb events and the interaction of those particles with material in the ALICE detectors. Figure 5.6 shows the production vertices (measured in the radial and z directions) for particles depositing energy in the EMCal. Figure 5.6 (left) shows the vertices for particles depositing energy before 30 ns, where the particles are produced in a cone from the interaction point, and Figure 5.6 (right) shows the vertices for particles depositing energy after 30 ns, where production occurs through out ALICE. The muon absorber is a significant source of background and this can be seen in the trapezium starting from z = -100 cm, r = 0 cm and moving towards negative values. The EMCal is located from r = 454 cm to 484 cm. In the second plot there is evidence of backscattering: particles hitting the L3 magnet beyond and scattering back through the EMCal.

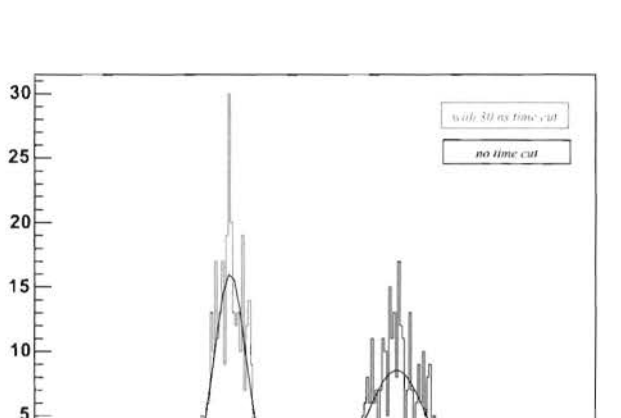

Figure 5.5: The total energy deposited in the EMCal in central Pb+Pb events with all the detectors (blue curve) and the same events with a 30 ns time cut (green curve)

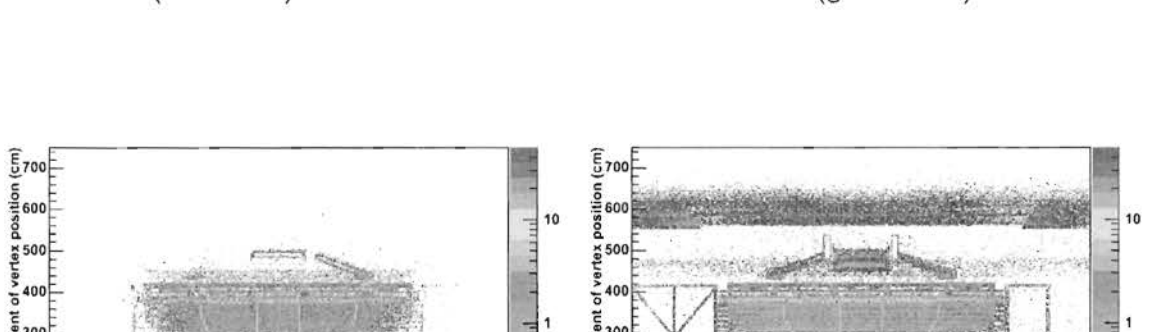

Figure 5.6: The production vertices (in projected into the radial and z directions) of particles depositing energy in the EMCal before 30n s (left) and after 30 ns (right), weighted by the deposited energy.

This large background from scattered particles at late times motivated the implementation of the integration time (called time cut) after [95]. The value for the time cut was determined from Figure 5.7: the ratio of integrated deposited energy from primaries that had their

momenta in the EMCal acceptance to those with momenta outside of the EMCal acceptance. This ratio decreases rapidly as the integration time increases. The exact value of the integration time to be implemented in the electronics is under still under discussion, but is expected to be in the range of 30-100 ns.

The energy deposited as a function of time was decomposed by particle types (Figure 5.7) where it was observed that this background at late times is caused by neutrons. Note that the neutrons continue depositing energy until $\sim 1\mu s$, well beyond the time shown in Figure 5.7.

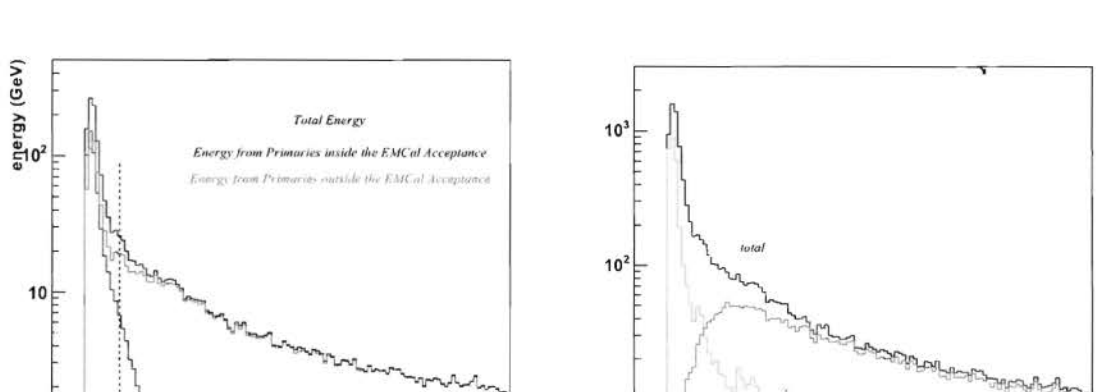

Figure 5.7: The deposited energy as a function of time. This can be split in the energy deposited by particles that were originally in the EMCal fiducial region and that deposited by particles outside the fiducial region (left). Alternatively, it can be shown as the energy deposited by different particles of which photons (orange) and neutrons (green) are shown as the dominant contributors. Note that the energy tail of the neutrons continues for an order of magnitude past the time scale of the plot.

5.4.1 Neutrons

The unexpectedly large energy deposited by neutrons led to further investigation. The large hydrogen content in the plastic scintillator means that high-energy neutrons knock out protons (like billiard balls) and these protons then deposit energy through ionisation. This is most efficient for high-energy neutrons, while low energy neutrons deposit energy through Compton scattering by producing electrons [96].

The Monte Carlo generator used in the simulations, GEANT, and the subroutine GHEISHA, is not optimised for the treatment of hadronic showers and underestimates high-energy hadronic energy depositions [97]. The GEANT tracking threshold is the energy below which particles are not tracked, and the neutrons are converted into two photons. Real neutrons would bounce around longer before converting. An energy threshold of 10 MeV was used in these simulations, which is appropriate for electromagnetic showers, but inappropriate for thermal neutrons. This means that the late time neutron background should be interpreted with caution. Additional simulations with FLUKA [98], a Monte Carlo generator with better treatment of hadronic interactions, are currently being investigated.

5.5 Tower Energy Cut

The 30 ns time cut reduces the tower occupancy to 60%, but this is not sufficient for clusterisation algorithms to easily reconstruct particles individually. A tower energy threshold,

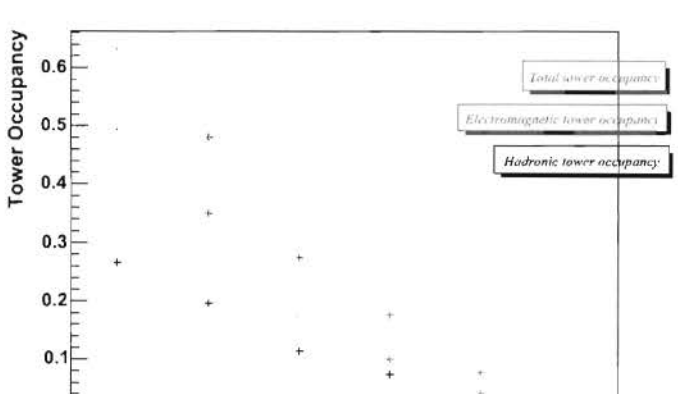

Figure 5.8: The fractional tower occupancy in the EMCal as a function of tower energy cut for central HIJING events with a time cut of 30 ns.

called the tower energy cut, can be used to artifically reduce the tower occupancy. The fraction of towers containing energy above the tower energy cut is shown in Figure 5.8 for different values of the tower energy cut. This total fraction is also split into hadronic and electromagnetic components. Once the minimum cut reaches 100 MeV, the tower occupancy drops to below 20% and the clusteriser can be expected to be able to reconstruct individual particles. It will shown in a later Section 6.1, that a much higher tower energy cut provides the best energy resolution.

This chapter has discussed simulation development together with some of the background contributions to photon measurements. This next chapter will discuss results on $\gamma - \pi^0$ discrimination.

Chapter 6

Results and Discussion

Clustering algorithms and methods of shower characterisation were discussed in Section 4.4. In this chapter, photon energy resolution calculated using the different algorithms (Section 6.1) is compared; shower shape analysis (SSA) is used to distinguish between photon and π^0showers (Section 6.2.1) and preliminary results on $\gamma - \pi^0$ discrimination in the EMCal (Section 6.3) are presented.

6.1 Photon Energy Resolution

The signal in the EMCal is significantly affected by background. The main contributions are from photon conversion (40% of photons convert before reaching the EMCal (see Figure 5.3) and Section 5.3) and particles, especially neutrons, from the underlying Pb+Pb event leave a large amount of energy in the calorimeter (see Figure 5.7). The background due to the underlying event can be significantly reduced by shortening the integration time, called the time cut (see Section 5.4), and by excluding particles with energies below a threshold from the clustering algorithm (see Section 5.5), called the tower energy cut. We now compare the photon energy resolution obtained using the four algorithm variants. Contamination caused by particles from the underlying Pb+Pb event degrades the energy resolution. The improvements gained by using a time cut and a tower energy cut are discussed. A correction for the shift of the mean measured energy due to the tower energy cut is introduced.

In this thesis the **energy resolution**, δE_{rel}, will be defined as the width of a Gaussian fit to the difference between the energy calculated for the cluster and the original photon energy (obtained from PYTHIA) scaled by the energy of the original photon, i.e.

$$\delta E_{rel} = \sigma\left(\frac{\Delta E}{E_{orig}}\right) \tag{6.1}$$

where $\Delta E = E_{clus} - E_{orig}$. The quantity $\frac{\Delta E}{E_{orig}}$ will be referred to as the **relative energy shift** of the cluster.

6.1.1 Comparison of energy resolution in the n-search and patch algorithms

This section presents photon energy resolution results for the different algorithms introduced in Section 4.4.1. The **patch algorithm** groups towers within a patch of fixed size centred on the highest energy tower. Patch sizes of nine towers (referred to as **3x3 patch**) and 25 towers (**5x5 patch**) were used. The **n-search** (or neighbour-search) algorithm groups together contiguous towers, by recursively adding the neighbours, above an energy threshold, of each tower in the cluster. The two variants of the n-search algorithm use different neighbour definitions. The **n-search vertex** considers towers with a common vertex to be neighbours, while the **n-search edge** considers towers with a common edge to be neighbours.

Numerous simulations were used to understand different effects. The third set of the simulations from Section 4.2.1: photons, simulated with only the EMCal, and embedded in central Pb+Pb events, were used for the energy resolution studies. Results are presented for photons with energies between 4 and 30 GeV. Below 4 GeV the background from particles from the Pb+Pb event makes the interpretation of the energy resolution difficult. Time cuts ranging from 20 ns to 1000 ns were used to assess the impact of the integration time on energy resolution.

The algorithms were tested using simulations with a 1 GeV cut on the clustering threshold [1] to reduce the number pure background clusters. Four different tower energy cuts were used for the n-search algorithms (from 100 MeV to 500 MeV). Information from the Monte Carlo event generation allowed selection of clusters containing energy deposited by one of the embedded photons.

The energy resolution for each case was obtained by fitting the relative cluster energy shift in 2 GeV bins of original particle energy. Two examples of these relative energy plots with their respective Gaussian fits are shown in Figure 6.1. The left figure illustrates a "bad" case with large values due to particles from the underlying Pb+Pb event. It uses the n-search vertex algorithm on low energy photons (8 - 10 GeV), with the maximum time cut (1000 ns) and a low tower energy cut (150 MeV). The figure on the right is an example of a "good" fit with little contribution from the underlying Pb+Pb event. It uses the n-search edge algorithm with the optimal time cut (30 ns) and a 500 MeV tower energy cut. In this case the distribution is clearly Gaussian with no tail. Note that the mean value of the relative energy shift is negative. This is caused by the tower energy cut and will be discussed further in Section 6.1.2.

Because the relative energy shift distribution often differs from a Gaussian (as in Figure 6.1 (a)), an iterative fit procedure was used to extract the Gaussian part of the energy resolution. This constrained the range of the current fit to $\{-3\sigma+\mu, 2\sigma+\mu\}$ using σ and μ obtained in the previous fit. The range was constrained asymmetrically because the underlying event increases the cluster energy, forming a tail at positive values. The fitting procedure was iterated four times to obtain the results presented in Figure 6.1. Note that the energy resolution obtained in this way does not take into account the full magnitude of the tail, hence the fits with large background underestimate the contribution of that background to energy resolution.

The fitting procedure was repeated for photons with energies between 4 and 30 GeV for each case introduced above. The resulting energy resolution as a function of energy was fitted to obtain an energy independent measure of the resolution (see Figure 6.2), using the following parametrisation to account for shower multiplicity fluctuations [77]:

$$\delta E_{RMS} = \sqrt{\left(\frac{A}{\sqrt{E}}\right)^2 + B^2} \tag{6.2}$$

Figure 6.2 shows the fit obtained for the n-search edge algorithm with a 30 ns time cut and a 500 MeV tower energy cut. The errors on the energy resolution shown are the errors from the Gaussian fit. The patch algorithm was implemented because it was expected to be insensitive to the large neutron background observed at late times, obviating the need to reduce the integration time. Figure 6.3 shows that the 3x3 algorithm gives very similar results with the 30 ns (solid) and 1000 ns (dashes) time cuts, while the total background energy in the EMCal doubles (see Figure 5.5). The 5x5 algorithm shows significantly worse energy resolution even with the 30 ns time cut. This is because photon showers contain less than nine towers on average (Figure 6.9(e)) so the additional 16 towers only increase the background contribution.

[1] The clustering threshold is minimum energy a tower must have to be the seed for a new cluster

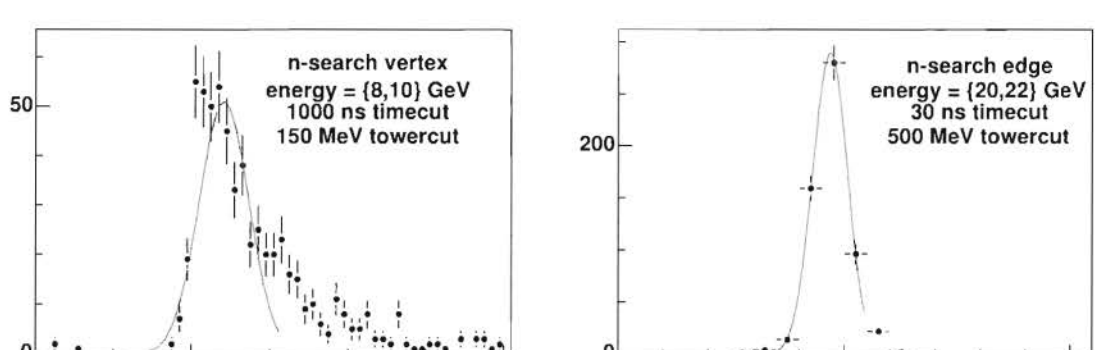

Figure 6.1: Examples of the fits used to determine the photon energy resolution. On the left is an example of a background contaminated fit using low energy photons (8 - 10 GeV) using the n-search vertex algorithm with the maximum time cut (1000 ns) and a low tower energy cut (150 MeV). On the right is an example of a fit showing little background contamination. It uses the n-search edge algorithm on high-energy photons (20 - 22 GeV), the optimal time cut (30 ns) and a high tower energy cut (500 MeV). Both were fitted using an iterative Gaussian fit, the details of which are discussed in the text.

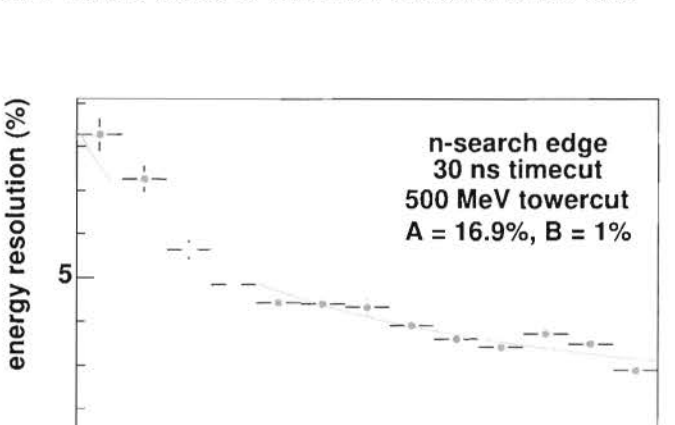

Figure 6.2: Energy resolution as a function of increasing photon energy for the n-search edge algorithm with a 30 ns time cut and a 500 MeV tower energy cut. The curve shown is a fit to Equation 6.2, the details of which are discussed in the text.

It is clear that the 3x3 patch algorithm consistently obtains better energy resolution than the 5x5 patch algorithm.

To compare the variants of the n-search algorithm, the slope parameter, A, from Equation 6.2 was plotted in Figure 6.4. Smaller slope parameters indicate better energy resolution. The n-search edge algorithm (blue) consistently provides better energy resolution than the n-search vertex algorithm (red) for each case. Increasing the tower energy cut improves the resolution in each case investigated, but has the least effect on the n-search edge algorithm. With a 500 MeV tower energy cut, all four cases, have a very similar energy resolution, because this cut removes almost all the background contribution. Shortening the time cut significantly improves the energy resolution by removing the contribution from the late-time neutrons.

The background effects were quantified by comparing the photon energy resolution results

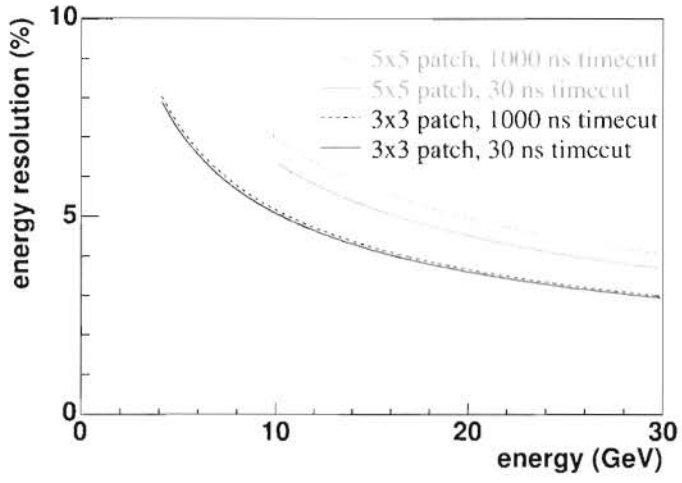

Figure 6.3: Energy resolution fits for the patch algorithm. The solid curves are fits using the optimal time cut (30 ns) and the dashed curves for a 1000 ns window. The 5x5 patch algorithm is in green and the 3x3 patch algorithm in blue. See text for discussion.

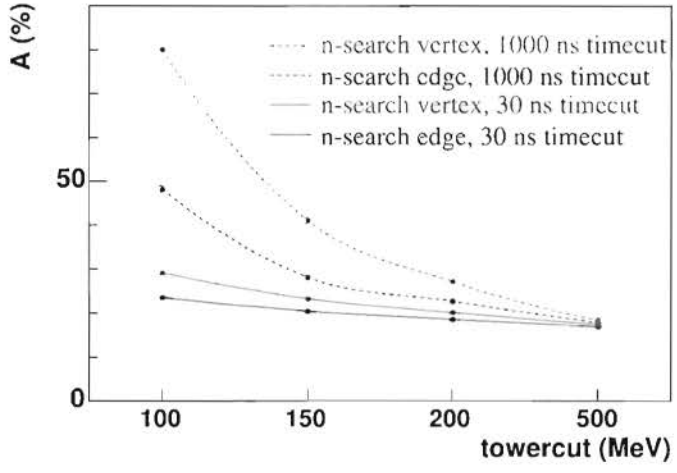

Figure 6.4: Comparison of the fit slope parameter for the n-search algorithms. The fit parameter, A (see Equation 6.2), is shown vs increasing tower energy cut for different versions of the n-search algorithm: n-search vertex (red) and n-search edge (blue) for both 30 ns (solid) and 1000 ns (dashed) time cuts.

with, and without, embedding the photons in Pb+Pb events (Figure 6.5). The dotted lines show that the energy resolution for single photons is slightly better with the 100 MeV tower energy cut (blue) than the 500 MeV tower energy cut (red), because with a larger tower energy cut more of the signal towers are cut out. This is reversed in the results on embedded photons, because the 500 MeV removes significantly more background, and this background is the dominant contribution to the energy resolution (cf. the solid curves).

Figure 6.6 compares the optimal cases for the four algorithms, with the 30 ns time cut. The results differ little between both the n-search algorithms and the 3x3 patch algorithm, with the 3x3 patch algorithm obtaining slightly better energy resolution. It is only with the 500 MeV tower energy cut that the energy resolution for the n-search algorithm is comparable to the patch algorithm. This 500 MeV tower energy cut limits the reconstruction of low energy

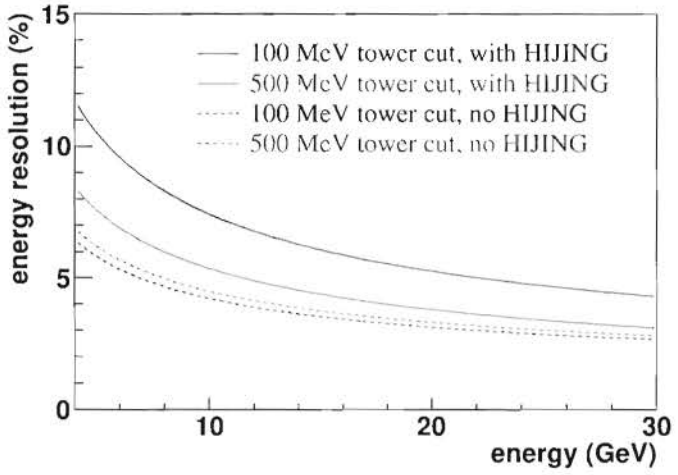

Figure 6.5: Energy resolution fits with (solid) and without (dashed) background for the n-search algorithm with tower energy cuts of 100 (blue) and 500 (red) MeV and a 30 ns time cut.

photons, which is an energy range in which the 3x3 patch algorithm could be very useful. Implementing refinements to the n-search algorithm, such as peak-finding and cluster-splitting, could reduce the number of clusters contaminated by overlapping background showers. This is expected to significantly improve the energy resolution of the n-search algorithm and extend the low momentum coverage.

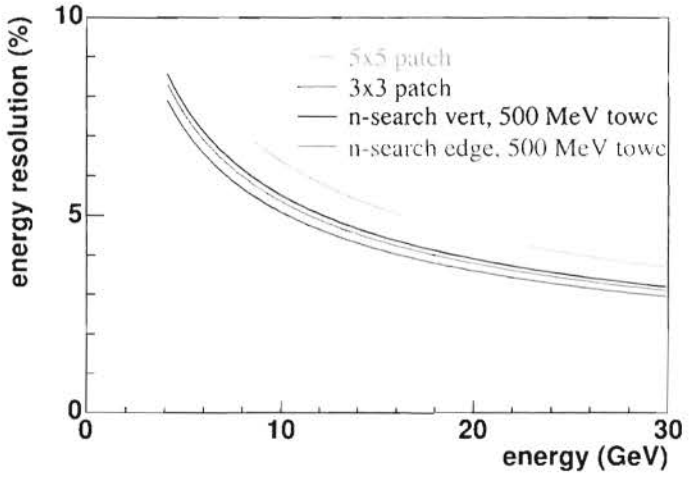

Figure 6.6: Parametrised energy dependence of the relative energy resolution for the best cases of the four algorithms. All the algorithms have a 30 ns time cut, and the n-search algorithms use a 500 MeV tower energy cut.

6.1.2 Energy correction for the Tower Energy Cut

The previous section showed that the tower energy cut reduces the contribution from particles of the underlying event to clusters. In addition to reducing contributions from the background, the cut excludes some of the lower energy towers from the signal. As the tower energy cut increases, more and more of the signal is removed and the mean of the relative energy distribution becomes increasingly negative (Figure 6.7 (a)), which shows the relative energy

shifts for single photons without any background. The shift in the mean of the relative energy is generally monotonic with energy and so it can be corrected with a polynomial fit. The mean energy shift for particles embedded in Pb+Pb events is very different (Figure 6.7 (b)) because the background tends to increase the total energy included in a cluster and this is typically a much greater effect than the shift due to the tower energy cut. For the 500 MeV tower energy cut, represented by the green curve, one sees that the means with the underlying Pb+Pb event approach the values of those without the underlying Pb+Pb event, especially at higher energies.

The precise details of this shift will be highly sensitive to the event multiplicity and hence the precise calibration can only be obtained from data. The energy dependence of the shifts was fitted with second order polynomials.

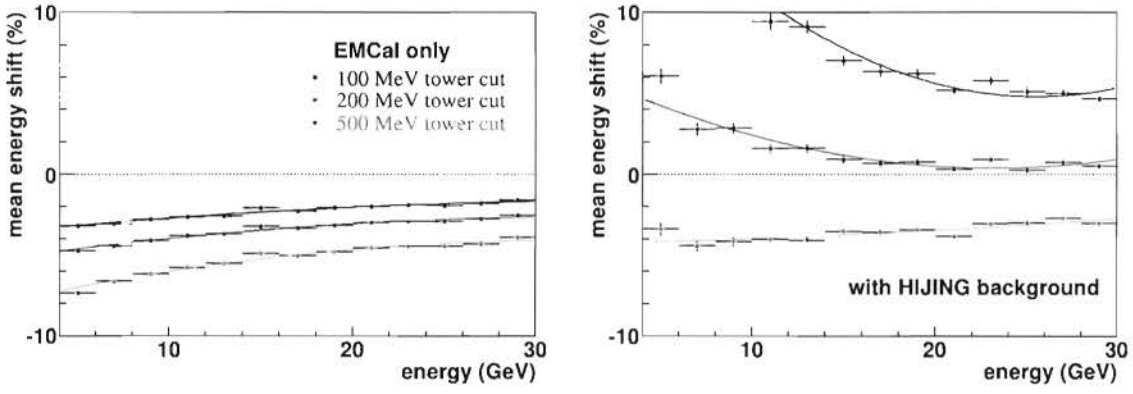

Figure 6.7: The means of the relative energy distributions for n-search edge algorithm for varying tower energy cuts. On the left is the result with only the EMCal and on the right is the result for photons embedded in a central Pb+Pb event.

6.2 γ-π^0 discrimination techniques

Three different methods of π^0 discrimination were introduced in Section 3.3.2: invariant mass analysis, shower shape analysis and the isolation cut. Their respective energy ranges of application are governed by the relationship between the opening angle between the decay photons and the size of the calorimeter's towers (see Figure 3.9). The distribution width shows that the opening angle is not only a function of energy, but also depends on how energy is divided between the two π^0s. This thesis will only discuss results from invariant mass and shower shape analysis as these are most appropriate to the EMCal acceptance.

Figure 6.8 shows how the percentage of π^0s being reconstructed as one or two clusters varies with energy. If a π^0 is reconstructed as two clusters, invariant mass analysis is the technique of choice, while with merged clusters, shower shape analysis is more appropriate. The green curves on the left hand plot show that at 14 GeV a π^0 is equally likely to be reconstructed as one or two clusters. Neutral pions with energy below 14 GeV are more likely to be reconstructed as two clusters and those with energy above 14 GeV are more likely to be reconstructed as a single cluster. Decreasing the tower energy cut means including lower energy towers in the cluster and hence lowers the energy at which the two photons become more likely to be reconstructed as a single cluster (9 GeV with a 100 MeV tower energy cut).

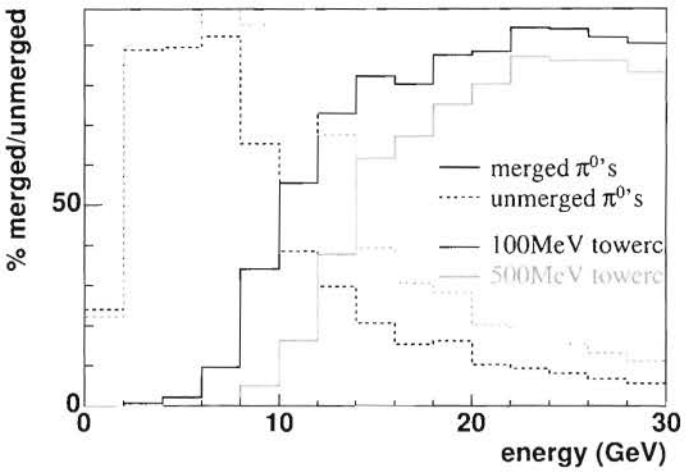

Figure 6.8: The percentage of π^0s producing two separate clusters (dashed) or one merged cluster (solid) using the n-search edge algorithms as a function of π^0 energy. These merged clusters are the background considered in the $\gamma - \pi^0$ discrimination studies using shower shape analysis.

6.2.1 Shower Shape Analysis

In the following, shower shape analysis will be explored and used to characterise the showers produced by photons and π^0 decay photons. The broadening of these showers due to photon conversions in the material from the other detectors and contamination from the Pb+Pb event will be discussed. Results on $\gamma - \pi^0$ discrimination using a momentum dependent cut will be presented.

6.2.1.1 Shower characterisation

In Section 4.4.2 parameters were introduced to characterise shower shapes:

- The lateral dispersion (Equation 4.6), which is the mean squared deviation of the towers from the shower centre, logarithmically weighted by the tower energy (Figure 6.9(c)) and measures the average shower radius.
- The lengths of the shower axes, λ_0 and λ_1 (Equation 4.12) are the eigenvalues of the shower shape tensor (see Equation 4.11) with $\lambda_0 > \lambda_1$ (Figures 6.9(a) and 6.9(b)).
- The sphericity (Equation 4.13) is the relative difference between the lengths of the shower axes (Figure 6.9(d)).
- The shower cell multiplicity (Figure 6.9(e)) is the number of towers that are included in the cluster.

The discriminatory power of each of these variables is demonstrated in Figure 6.9, where the shower shape parameters for photons and neutral pions with energies between 14 and 16 GeV, with no tower energy cut and without the Pb+Pb event are shown. It can be seen that λ_0 provides the best separation, as expected, because it provides the most direct measure of the opening angle between the π^0 decay photons. Additionally, it is uncontaminated by shower fluctuations perpendicular to the axis along the opening angle, in contrast to the dispersion and the sphericity.

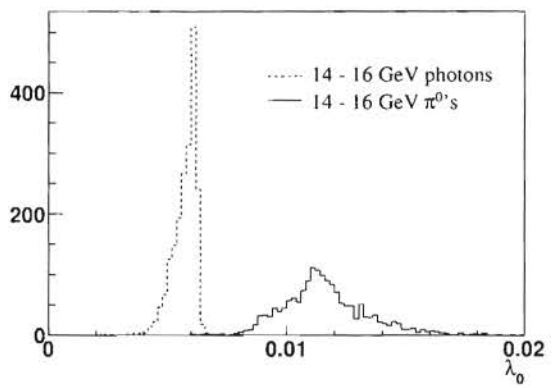

(a) First eigenvalue of the shower shape tensor (λ_0)

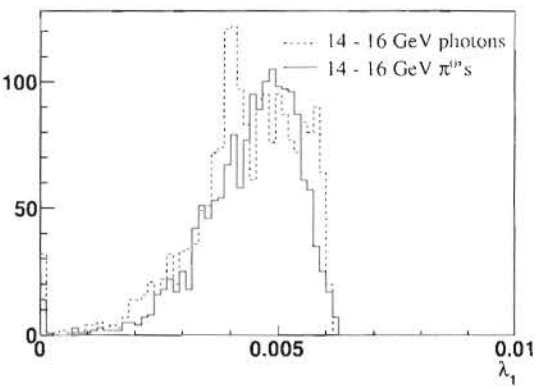

(b) Second eigenvalue of the shower shape tensor (λ_1)

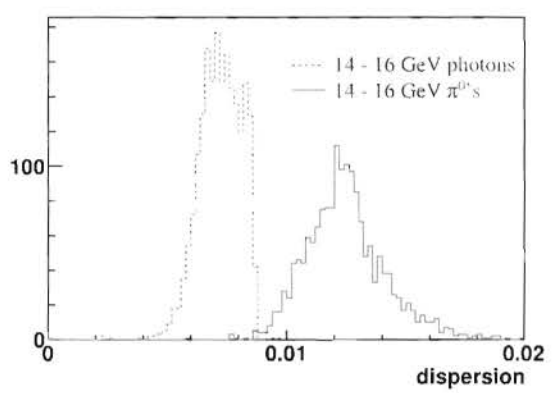

(c) Dispersion

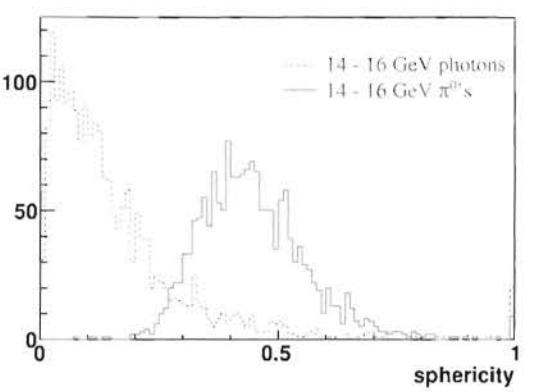

(d) Sphericity

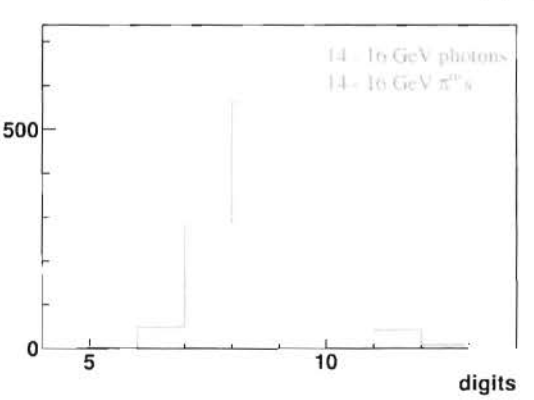

(e) Number of towers per cluster

Figure 6.9: Shower shape parameter for photons and π^0s with energy between 14 and 16 GeV, with only the EMCal simulated, using a 100 MeV tower energy cut and the n-search vertex algorithm. See text for further discussion.

In Figure 6.10 the dispersion, λ_0 and the sphericity are compared for photons and pions embedded in Pb+Pb events. The distributions, and most noticeably the sphericity, are broadened by contributions from particles in the Pb+Pb event. The tower energy cut, 500 MeV, reduces the contribution from the underlying Pb+Pb event significantly. An important effect, caused by the addition of background, is the increase in the photon dispersion and λ_0 values.

The use of λ_0 in $\gamma - \pi^0$ discrimination will now be pursued. This parameter was selected because of the small spread for photons and the larger separation between photons and π^0s than the dispersion. The next section will explore the different background contributions to λ_0 and determine the optimal λ_0 cut for $\gamma - \pi^0$ discrimination.

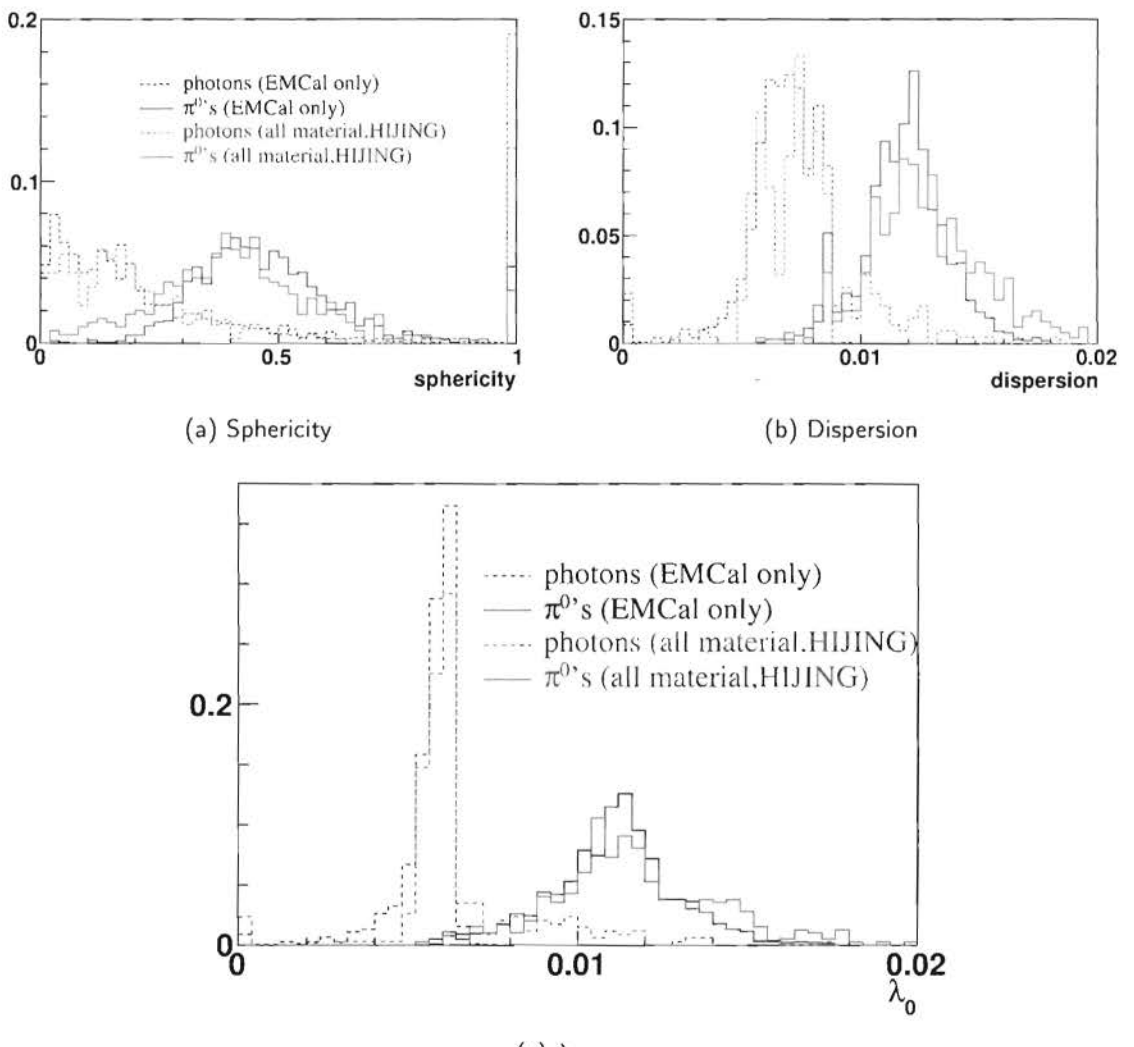

(a) Sphericity

(b) Dispersion

(c) λ_0

Figure 6.10: The effect of the background on the shower shape parameters. Results are shown for 14-16 GeV photons (dashed) and π^0s (solid) with only the EMCal (black) and from embedding in a central Pb+Pb event (red). Results using the n-search edge algorithm with a 500 MeV tower energy cut and a 30 ns time cut.

6.2.1.2 SSA analysis with second cluster moment, λ_0

It was shown in the previous section that the second cluster moment, λ_0, is the most robust shower shape parameter in the high multiplicity environment of heavy-ion collisions. It is largely unaffected by the 40% of photons converting in the material before the EMCal (Figure 6.11

(left)) but more altered when embedding the particles in a Pb+Pb event (Figure 6.11 (right)). Both these effects decrease when the tower energy cut is raised, making λ_0 a very clean observable.

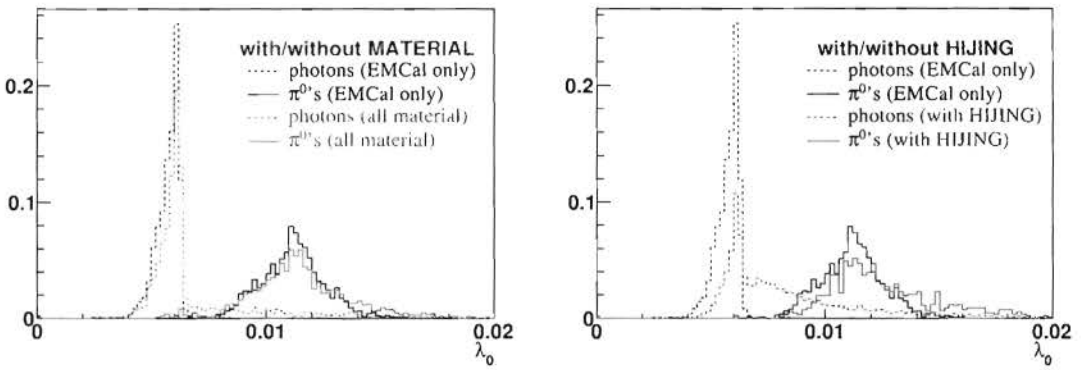

Figure 6.11: Comparison of the λ_0 distribution for photons and merged π^0s with and without the conversions in the ALICE detectors (left) and the underlying event (right). Results using the n-search edge algorithm, with a 200 MeV tower energy cut, for photons and π^0s with energies between 14 and 16 GeV.

Figure 3.9 showed how the distance between the decay photons from a π^0 decreases with increasing energy and λ_0 decreases accordingly. Figure 6.12 shows that λ_0 for π^0s that have two separate clusters (orange) is approximately energy independent, with a mean value just below 0.006. For merged clusters (green), λ_0 decreases strongly with energy until it becomes equal to that of the single photons at a p_T of about 60 GeV.

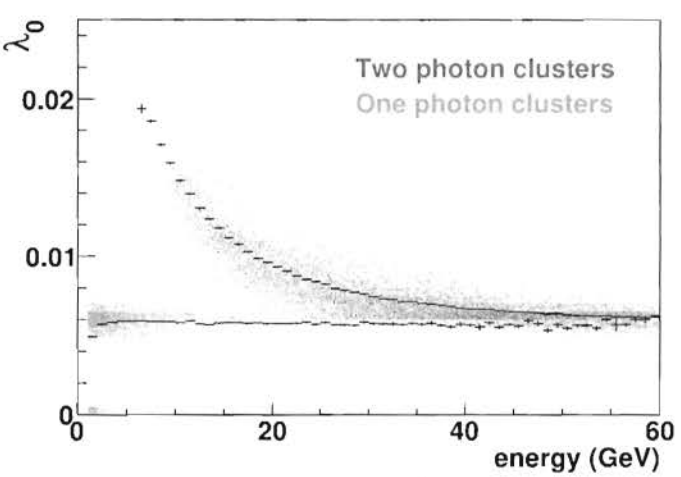

Figure 6.12: The second cluster moment, λ_0, for π^0s as a function of energy. The photons that form two separate clusters have an energy independent λ_0 value (orange), while the photons that merge into one cluster have a large λ_0 value (green), falling steeply with increasing cluster energy. The mean values of the λ_0 distributions, for each case are plotted in black. The distance between these mean values provides an indication of the $\gamma - \pi^0$ discrimination capabilities of the EMCal.

Since λ_0 for π^0s decreases significantly with energy, the λ_0 cut was optimised in 2 GeV energy bins, by maximising the significance. The significance was defined to minimise the relative errors in the final measurement as estimated by:

$$Sig = S/\sqrt{S+B} \tag{6.3}$$

where

- S = number of photons accepted by the λ_0 cut
- B = number of π^0s accepted by the λ_0 cut

The n-search edge algorithm was used in this analysis because energy resolution studies showed that it produced better results than the n-search vertex algorithm (see Section 6.1). The patch algorithms were not considered because they are unsuitable for use on merged clusters due to the fixed patch size.

Three different tower energy cuts were applied, because although the 500 MeV tower energy cut obtains the best energy resolution (Figure 6.5), it is expected that lowering the tower energy cut would increase the sensitivity to shower shapes. It turns out that the effect of the background is large and the 500 MeV tower energy cut consistently obtains a greater significance (see Figure 6.14 which compares the significance obtained for the three cuts).

Figure 6.13 shows the λ_0 cut value as a function of energy for the three tower energy cuts, for maximum significance. Below 10 GeV, the results should be interpreted with caution because there are very few π^0s reconstructed as a single cluster, but the larger λ_0 values are representative of the shower broadening of low-energy photons. The 500 MeV tower energy cut (blue curve) has a smaller λ_0 cut than the other tower energy cuts, because it has the smallest background contribution to the photon λ_0 distribution. At high p_T there is a sharp rise in the optimal λ_0 cut, which occurs first for the 100 MeV tower energy cut at approximately 35 GeV. This is the value at which the λ_0 distributions for the photons and the π^0s overlap entirely and one cannot use shower shape analysis to discriminate. Increasing the tower energy cut increases the energy range of SSA by removing more of the background, which broadens the photon λ_0 distribution.

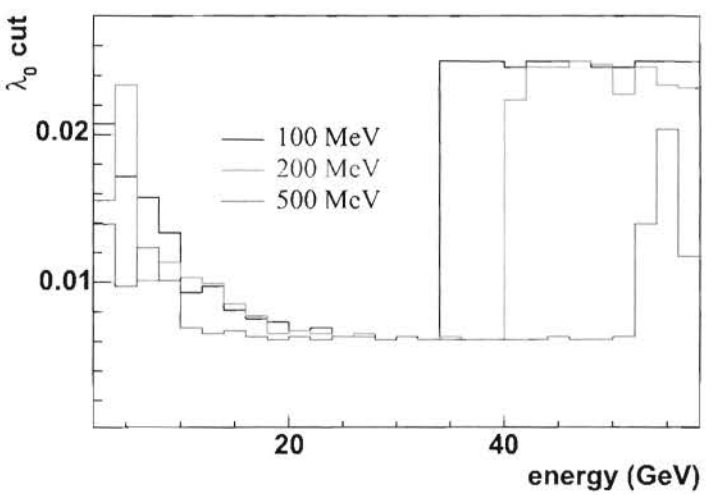

Figure 6.13: The λ_0 values that maximise the significance, calculated in 2 GeV energy bins for three different values of the tower energy cut.

Excellent photon efficiency is obtained with the λ_0 cut (see Figure 6.15) with small contamination from π^0s. This π^0 contamination increases with energy as the λ_0 distribution moves closer to the photon λ_0 distribution. The photon efficiency was defined to be the number of photons accepted by the λ_0 cut divided by the total number of photons simulated, with an analogous definition for the π^0s. Note that this underestimates the contamination from π^0s somewhat by assuming a 100% efficiency for the invariant mass cut. At 50 GeV,

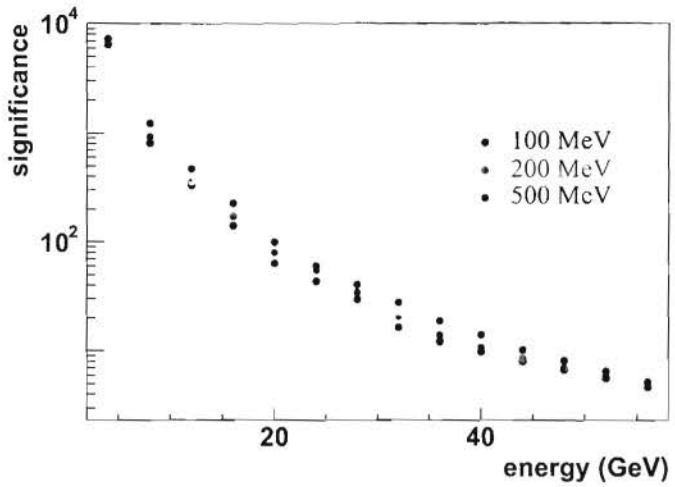

Figure 6.14: The significance of $\gamma - \pi^0$ discrimination for photons not showering before the calorimeter, and merged π^0s (the showers from the two photons overlap) with p_T dependent λ_0 and varying tower energy cuts in central Pb+Pb events in one ALICE year. See text for details.

where one reaches the edge of the range of applicability of $\gamma - \pi^0$ discrimination, the signal becomes rapidly contaminated with π^0s. These efficiency and contamination plots will be scaled by NLO pQCD cross-sections to obtain realistic predictions for photon and π^0 spectra after applying SSA.

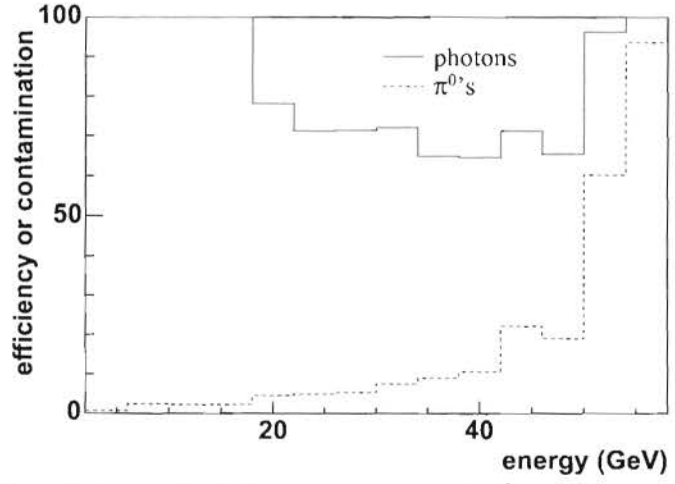

Figure 6.15: The efficiency of photon acceptance and π^0 acceptance is shown for single photons, which do not shower before the calorimeter, and merged π^0s (the showers from the two photons overlap) with p_T independent λ_0 cut of 0.007 and a minimum tower energy cut of 500MeV within central Pb+Pb events.

This section has shown that λ_0 with a 500 MeV tower energy cut provides an excellent method for discriminating between photons and π^0s, with energies between 10 and 50 GeV, even within the large background from Pb+Pb events.

6.2.2 Invariant Mass Analysis

The previous section discussed how a λ_0 cut can be applied to discriminate between photons and merged π^0s. Figure 6.8 shows that below 13 GeV more than 50% of the π^0s are re-

constructed as two separate clusters in the EMCal. It will now be shown that invariant mass analysis can be used to eliminate a significant proportion of these clusters.

Figure 6.16 provides a first look at invariant mass analysis. Photons were simulated with all the material from the ALICE detectors and embedded in central Pb+Pb events. The n-search edge algorithm with a 500 MeV tower cut and a 1 GeV clustering seed, was run to produce clusters. A 2 GeV cluster energy threshold [2] was used to reduce the low momentum background contribution. The λ_0 cuts from Figure 6.13 were applied to identify photon clusters. Due to the limited statistics, there were insufficient π^0 candidates to exhibit a peak, so the invariant mass was recalculated with the requirement that only one of the photon candidates was selected by the λ_0 cut.

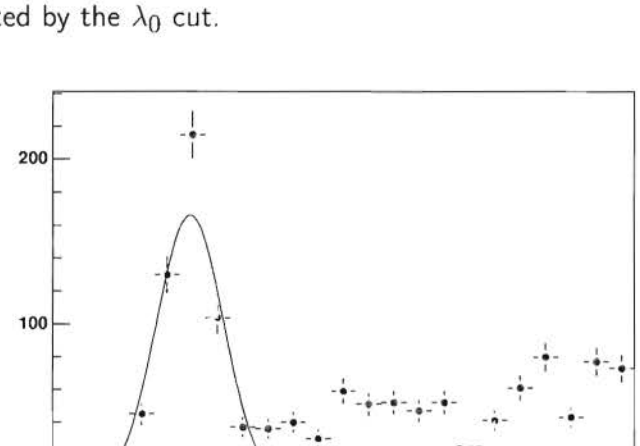

Figure 6.16: The invariant mass peak obtained for π^0s embedded in central HIJING events using the optimised λ_0 cut on one of the photons. The n-search edge algorithm used a tower cut of 500 MeV, a clustering seed of 1 GeV and a cluster energy cut of 2 GeV.

The invariant mass distribution obtained with the λ_0 cut on one of the photons is shown in Figure 6.16, which was then fitted with a Gaussian distribution. There is still contamination due to the underlying event, that possibly could be reduced by applying the λ_0 cut to the second photon candidate. This result shows that shower shape analysis additionally rejects many hadronic showers. It should be treated as preliminary as it considers a sample of events enhanced by embedding π^0s and further work is needed to demonstrate the full range and limitations of its applicability.

6.3 $\gamma - \pi^0$ discrimination results

Section 6.2.1 discussed the application of SSA to $\gamma - \pi^0$ discrimination. We now present those results scaled by predicted cross-sections from Figures 2.10(a) and 2.10(b) and discuss the enhancement of the γ/π^0 ratio obtained from SSA.

The efficiencies from Figure 6.15 were scaled by the respective photon and π^0 cross-sections (see Figure 2.10) and presented in Figure 6.17. The black points show the number of photons that will be accepted in one ALICE year using the λ_0 cut and the red points show the number of π^0s that will be included by that same cut.

The ratio of the number of photons to the number of π^0s after applying the λ_0 cut (the blue curve in Figure 6.18) is compared to the γ/π^0 ratio expected. The peak between 10 and

[2] The cluster energy threshold was the minimum cluster energy for a cluster to be used in the analysis

20 GeV covers the energy range to which the analysis is best suited, because the π^0 decay photons are well separated. For photons with energies approximately 20 GeV the γ-π^0ratio is enhanced by a factor of 50 relative to the theoretical prediction (Fig 2.10(b)). The overlap of the photon and neutral pion λ_0 distributions increases with energy and reduces this ratio. The γ/π^0 ratio at high energies is expected to depend on the event multiplicity, which will only be determined from data.

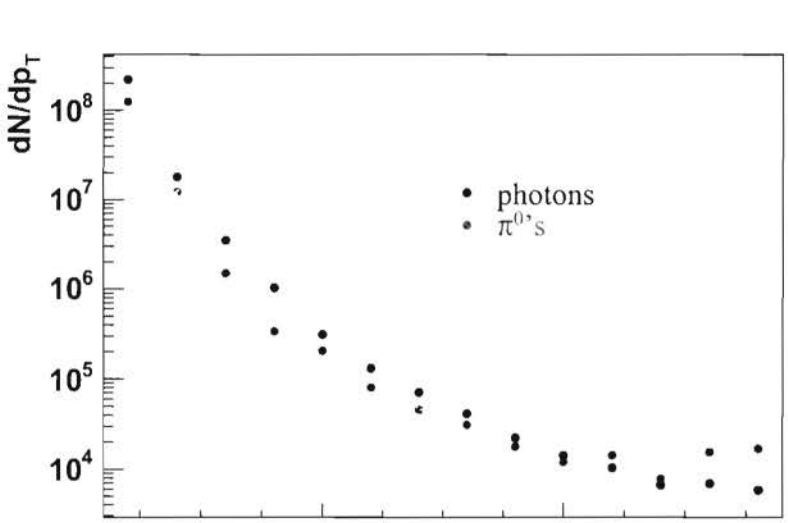

Figure 6.17: The photon yield (black) per ALICE year ($10^6 s$) in minimum bias Pb+Pb collisions as a function of p_T obtained using the optimised λ_0 cut compared to the contamination from merged π^0s (red). The invariant cross-sections are NLO pQCD predictions with the CTEQ5M structure function, EKS98 for nuclear shadowing and an energy loss parameter.

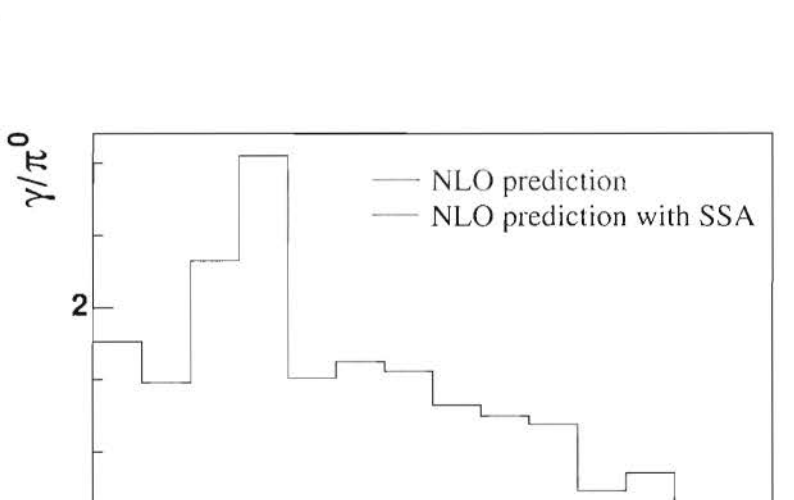

Figure 6.18: Expected enhancement of the γ/π^0 ratio (blue) after applying SSA to the ratio predicted by NLO pQCD calculations (red) in Figure 2.10(b).

It has been shown that the n-search edge algorithm consistently produces better results than the n-search vertex algorithm; and that the 500 MeV tower energy cut improves both the energy resolution and the $\gamma - \pi^0$ discrimination capabilities. The 3x3 patch algorithm provides slightly better energy resolution than the n-search algorithm and it seems likely that it is the preferred algorithm for reconstructing low energy photons. Shower shape analysis can be used in the EMCal in heavy-ion collisions to provide $\gamma - \pi^0$ discrimination for particles with energies between 10 and 50 GeV (Figure 6.17).

Chapter 7

Conclusion

This thesis has demonstrated that the EMCal, with an acceptance seven times larger than PHOS, can be used to significantly extend the high-p_T photon measurements of the ALICE experiment in heavy-ion collisions at the LHC.

Photon energy resolution was calculated using four cluster-finding algorithm variants, which were modified to account for the large background in Pb+Pb collisions at 5.5 TeV. The best energy resolution was obtained with the 3x3 patch algorithm (5% at 10 GeV and 3% at 30 GeV).

The n-search algorithm was used to characterise photon and neutral pion shower shapes, and a cut based on their shower shape differences was used to reduce the contamination by neutral pions in the direct photon spectrum. The n-search edge algorithm consistently obtained superior results to the n-search vertex algorithm. The technique of $\gamma - \pi^0$ discrimination enhanced the γ/π^0 ratio by a factor of 50 at 20 GeV.

A measurement of direct photon spectrum can be used to test theoretical predictions about photon production and the measurement of γ-jet fragmentation functions should provide a better understanding of parton energy loss in a hot dense medium.

Chapter 8

Outlook

This thesis presented results for the reconstruction and identification of photons with energies between 10 and 50 GeV. Methods to improve the p_T coverage and physics measurements will now be discussed.

8.1 Extending the EMCal photon p_T range

The low p_T coverage can be extended by implementing cluster splitting and high p_T coverage by an isolation cut.

Preliminary results for photons with energies below 10 GeV were presented, but the 500 MeV tower energy cut needed by the current algorithm limits the low-p_T photon reconstruction. Clusters containing energy from more than one particle can be identified by implementing peak-finding algorithms. Provided that the shower profile is well understood, fits to a shower containing more than one particle can be used to apportion the energy into two separate clusters. In principle, a cluster-splitting algorithm should be able to remove a large proportion of the contamination from particles from the underlying event, and therefore reduce the tower energy cut used.

The photon reconstruction techniques have no upper energy limit, but the photon candidate spectrum becomes increasing contaminated by the decay photons from π^0s as the opening angle between the decay photons decreases with energy. These high-energy π^0s are invariably produced in jet fragmentation and therefore are accompanied by other particles produced in the fragmentation. An *isolation cut* can be used to reject these high-energy π^0s by considering a cone around the photon candidate. If there are other particles within that cone, the photon candidate is rejected as a direct photon. Isolation cuts also can be used to separate the prompt photons from the bremsstrahlung photons.

Isolation cuts have been used in p+p collisions, but in heavy-ion collisions their application is complicated by the high multiplicity of the underlying Pb+Pb event. In jet fragmentation the leading particle typically has 20% of the jet energy, therefore the energies of the remaining jet particles soon fall below the background. Energy fluctuations in the underlying Pb+Pb event (9% in 5% central collisions) complicate the choice of the energy threshold for the cone. The efficiency of the isolation cut is strongly dependent on the precise details of jet fragmentation, which are not well constrained by either PYTHIA or p+p collisions. This makes the interpretation of direct photon results using an isolation cut difficult.

8.2 Physics measurements with photons

The motivation for high-p_T photon studies in the EMCal was to measure parton energy loss directly with γ-jet fragmentation functions. We present here a first look a γ-jet fragmentation function, to show the necessity of accurate energy measurement.

Fragmentation functions were introduced in Section 2.5 and are used to study jet fragmen-

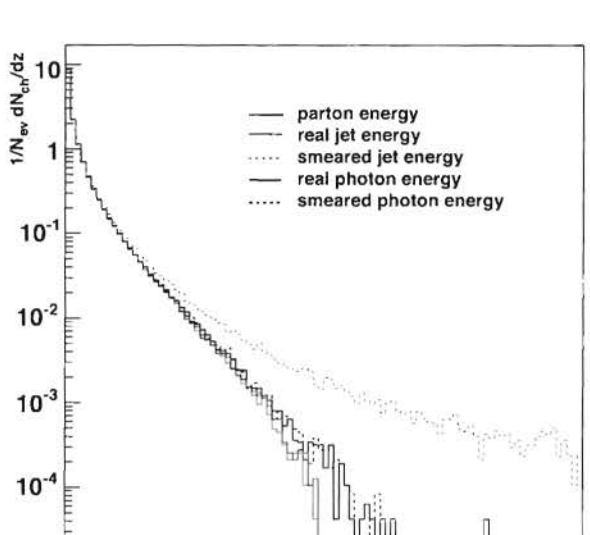

Figure 8.1: Fragmentation functions for 100 GeV jets from PYTHIA without background from the Pb+Pb event. The histograms are calculated with different values for the energy. The solid histograms use energy values from PYTHIA: parton energy (blue), photon energy (black), jet energy (red). The dashed histograms were obtained by smearing the photon (3.5 %) and jet energies (40 %) by the expected EMCal energy resolution. See text for details.

tation. Figure 8.1 shows an example of a fragmentation function for 100 GeV jets from pure PYTHIA simulations (no background from the underlying event). The different histograms measure the jet energy in different ways. The true fragmentation function (blue histogram) uses the parton energy. The red dashed histogram smears the jet energy by a 40% energy resolution [1] and the black dashed curve smears photon energy by 3.5%. The figure shows that imprecise energy measurements have a large impact on fragmentations functions and could very well obscure the changes to the fragmentation function from the medium.

Other intended high-p_T photon measurements include jet energy calibration and correlations. The correlations, including $\gamma - \gamma$ and $\gamma - \pi^0$, can measure jet energy loss even with the inclusion of bremsstrahlung photons **??**.

[1] A jet energy resolution of 40% is somewhat conservative: a more accurate estimate would be 25-30% [99]

Appendix A

Kinematics

Collision energy and geometry For collider experiments the initial state is usually specified as the centre of mass energy per nucleon, 5.5 TeV at the LHC. The final state is fully characterised by the momenta $\overrightarrow{p} = (p_x, p_y, p_z)$ and the mass, m, or energy, E of all particles. These three quantities are related by [1]

$$E = \sqrt{m^2 + p^2} \tag{A.1}$$

Figure A.1 illustrates the geometry of a nucleus-nucleus collision. The grey shaded regions shows the nucleons that are the *participants* in the collision. The nucleons in the unshaded regions are referred to as *spectators*. The impact parameter, b, is the distance between the centres of the nuclei. The collision centrality is increases as the impact parameter decreases.

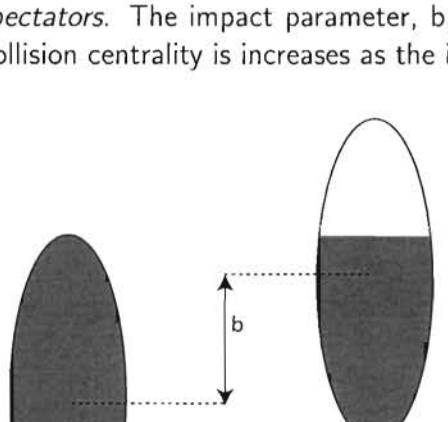

Figure A.1: An illustration of a nuclear collision. The shaded regions indicate the nucleons that participate in the collision. The impact parameter, b, is the distance between the centres of the nuclei and determines the centrality of the collision.

Transverse Momentum The collisions are approximately symmetric about the beam direction therefore the momentum can be reduced to the longitudinal, (p_z), and transverse momentum, $p_t = \sqrt{p_x^2 + p_y^2}$, with the z axis lying along the beam direction.

Rapidity Alternative variables are the transverse mass, m, and rapidity, y defined by

$$y = \frac{1}{2} \ln \frac{E + p_z}{E - p_z} \tag{A.2}$$

[1] Natural units are used throughout this thesis, with the speed of light c and Planck's constant $\hbar$ both set to one. Energy will be given in GeV.

and

$$m_t = \sqrt{m^2 + p_t^2} \tag{A.3}$$

The rapidity is additive under Lorentz boosts along the z-axis, which means that rapidity differences are unchanged, i.e. Lorentz invariant. The range in rapidities of the produced particles varies with the collision energy. At the LHC particles will be produced with $|y| < 8$.

Pseudorapidity In experiments, detected particles are not always identified. Both the momentum and the energy are needed to calculate the rapidity, but in high-energy experiments the mass can often be negligible when compared to the momentum. The *pseudorapidity*, η, approximates the energy with the momentum and can be calculated by the following:

$$\eta = \frac{1}{2} \ln \frac{p + p_L}{p - p_L} = \frac{1}{2} \ln \frac{1 + \cos\theta}{1 - \cos\theta} = \ln \cot \frac{\theta}{2} \tag{A.4}$$

For massless particles, the pseudorapidity will be identical to the rapidity. For massive particles, it can be used to approximate the rapidity for large momenta. Equation A.4 shows the pseudorapidity is related to angle of particle-emission relative to the beam axis.

For a full discussion of the kinematics of high-energy nuclear collisions see [100].

Glossary

γ-jet A leading order pQCD process in which a photon and a parton are emitted back-to-back in a hard scattering.

λ_0 The second cluster moment. A measure of the maximal width of a cluster

μ_B The baryonic chemical potential is a measure of the excess of baryons over anti-baryons in a system

Active material In this thesis, the material in the EMCal that converts deposited energy into light will be referred to as the active material.

AGS Alternating Gradient Synchrotron. A previous heavy-ion experiment at Brookhaven.

ALICE A Large Ion Collider Experiment. The dedicated heavy-ion experiment at the LHC

Bremsstrahlung photons There are two types of bremsstrahlung photons in heavy-ion collisions: either produced directly in NLO pQCD processes or through the multiple scattering of a hard parton in a dense medium.

Cluster A grouping of the towers with energy deposits in the calorimeter.

Dead material In this thesis, the material in the EMCal that does not convert deposited energy into light will be referred to as the dead material.

Decay photons The photons produced in the decay of a π^0The decay photon are the predominant background to the direct photon signal.

Digit A Digit is the energy deposited in a tower (like an SDigit), but convoluted with additional detector effects.

Direct photons Photons produced at early times during the system evolution. These include all photon sources except photons produced in the decays of particles such as π^0s.

EMCal The proposed Electromagnetic Calorimeter for the ALICE experiment.

Fragmentation function A jet fragmentation function is a characterisation of the momentum distribution of particles within a jet.

HG Hadron Gas.

HIJING Heavy Ion Jet INteraction Generator. A computer program, based on PYTHIA, used to simulate Pb+Pb collisions.

Hit A Hit is the energy deposited by a single particle in a tower.

Isolation cut An experimental technique to reduce the contamination of the direct photons by π^0s and bremsstrahlung photons produced in jet fragmentation. This achieved by rejecting direct photons candidates if there are other particles inside a cone centred on the photon candidate.

Jet A jet is a localised group of particles produced in the fragmentation of a high-energy parton.

LHC The Large Hadron Collider is a particle accelerator, which is being built at CERN.

LO pQCD Perturbative QCD calculation including terms up to leading order in α_S

Merged cluster If the two π^0 decay photons are reconstructed as a single cluster by the clustering algorithm, that cluster is termed a merged cluster.

MIT bag model A phenomenological description of quark confinement.

Molière radius A circle of Molière radius 1 contains 95% of the shower energy.

N-search algorithm The neighbour-search clustering algorithm groups together contiguous towers. Two variants were used: the n-search vertex algorithm and the n-search edge algorithm.

N-search edge algorithm A variant of the neighbour-search clustering algorithms that groups together towers with common edges.

N-search vertex algorithm A variant of the neighbour-search clustering algorithms that groups together towers with either common edges or vertices.

Neighbour Two different ways of selecting adjacent towers were used. The n-search edge algorithm defines neighbours as two towers with a common edge. The n-search vertex algorithm defines neighbours as two towers with either a common edge or a common vertex.

NLO pQCD Perturbative QCD calculation including terms up to next-to-leading order in α_S

Nuclear interaction length,λ_{int} The average distance a high-energy hadron has to travel in a material before a nuclear interaction occurs

Opening angle The angle between the momenta of two photons produced in the decay of the neutral pions.

Patch algorithm A Clustering algorithm that groups together all towers within a patch centred on the highest energy tower. Two patches were used: consisting of 3x3 and 5x5 towers.

PHOS The Photon Spectrometer, one of the ALICE detectors, is a lead-glass calorimeter designed for prompt photon detection.

Projective Tower A projective tower is oriented with the length lying along a radial line from the interaction point.

Prompt photons Prompt photons are produced in a hard QCD processes: Compton scattering of gluons and quark anti-quark annihilation.

QCD Quantum Chromodynamics. A non-Abelian gauge theory that describes the strong interaction.

QGP The Quark-Gluon Plasma is a state of matter that consists of deconfined quarks and gluons, thought to have existed shortly after the Big Bang.

Radiation length The distance over which an electron loses, on average, 63.2% of its energy through bremsstrahlung

Relative energy shift The difference between the original photon and reconstructed photon energies divided by the original photon energy.

RHIC The Relativistic Heavy-Ion Collider located at Brookhaven.

Sampling fraction A correction factor to account for energy deposited in the dead material of the calorimeter. The sampling fraction was calculated from photon simulations by comparing the original photon energy to the energy recorded by the calorimeter.

SDigit An SDigit is the energy deposited in a tower, summed over all particles depositing energy in that tower (cf. Hit).

Shower maximum The depth into a detector when the rate of energy deposition is a maximum.

Shower shape tensor A tensor whose elements are the variances of the shower in the η and ϕ directions.

SSA Shower Shape Analysis. A method for characterising shower shapes.

Thermal photon Photons produced during multiple scattering in a hot medium. The momentum distribution of thermal photons reflects that of the particles in the medium and therefore the medium temperature.

Tower energy cut A cut used to reduce the background from the Pb+Pb event to clusters. Towers with energies below the tower energy cut are excluded from the cluster.

Bibliography

[1] E. Rutherford, Phil. Mag. 21 (1911) 669.

[2] J. Chadwick, Nature 129 (1932) 312.

[3] E. Rutherford, Phil. Mag. 37 (1919) 581.

[4] M. Gell-Mann, Phys. Lett. 8 (1964).

G. Zweig, An SU3 model for strong interaction symmetry and its breaking, CERN preprint: CERN-TH-401, 1964.

[5] Y. Ne'eman, Nucl. Phys. 26 (1961) 222.

M. Gell-Mann, The Eightfold Way: A Theory of Strong Interaction Symmetry, Caltech report: CTSL-20. Reprinted in Frontiers in Physics, 1964, 1961.

[6] S. Eidelman and . others (Particle Data Group), Physics Letters B 592 (2004) 1+.

P.F. Smith, Annual Review of Nuclear and Particle Science 39 (1989) 73.

L. Lyons, Phys. Rept. 129 (1985) 225.

M. Marinelli and G. Morpurgo, Phys. Rept. 85 (1982) 161.

[7] K. Wilson, Phys. Rev. D 10 (1974) 2445.

[8] J. Bjorken, Phys. Rev. 179 (1969) 1547.

R. Feynman, Phys. Rev. Lett. 23 (1969) 1425.

[9] D.J. Gross and F. Wilczek, Phys. Rev. Lett. 30 (1973) 1343.

H.D. Politzer, Phys. Rev. Lett. 30 (1973) 1346.

[10] D.J. Gross and F. Wilczek, Phys. Rev. D8 (1973) 3633.

H.D. Politzer, Phys. Rept. 14 (1974) 129.

[11] G. Lemaître, Ann. Soc. Sci. Bruxelles 47A (1927) 49.

[12] A. Chodos et al., Phys. Rev. D9 (1974) 3471.

[13] N. Cabibbo and G. Parisi, Phys. Lett. B59 (1975) 67.

[14] R.J. Fries and B. Muller, Eur. Phys. J. C34 (2004) s279, nucl-th/0307043.

[15] QCD thermodynamics: The numerical study of strongly interacting matter under extreme conditions, 2001, Prepared for NIC Symposium 2001, Julich, Germany, 5-6 Dec 2001.

[16] Z. Fodor and S.D. Katz, JHEP 03 (2002) 014, hep-lat/0106002.

[17] Z. Fodor and S.D. Katz, JHEP 04 (2004) 050, hep-lat/0402006.

[18] T.D. Lee and G.C. Wick, Phys. Rev. D9 (1974) 2291.

[19] J.C. Collins and M.J. Perry, Phys. Rev. Lett. 34 (1975) 1353.

[20] E.V. Shuryak, Sov. Phys. JETP 47 (1978) 212.

[21] E.V. Shuryak, Phys. Lett. B78 (1978) 150.

[22] H.G. Ritter and X.N. Wang, editors, Ultra-relativistic nucleus-nucleus collisions. Proceedings, 17th International Conference, Quark Matter 2004, Oakland, USA, January 11-17, 2004 Vol. G30, 2004, Prepared for 17th International Conference on Ultra Relativistic Nucleus-Nucleus Collisions (Quark Matter 2004), Oakland, California, 11-17 Jan 2004.

H. Gutbrod, J. Aichelin and K. Werner, editors, Quark matter 2002. Proceedings, 16th International Conference on ultrarelativistic nucleus nucleus collisions, QM 2002, Nantes, France, July 18-24, 2002 Vol. A715, 2003, Prepared for 16th International Conference on Ultrarelativistic Nucleus-Nucleus Collisions: Quark Matter 2002 (QM 2002), Nantes, France, 18-24 Jul 2002.

[23] J.D. Bjorken, Phys. Rev. D27 (1983) 140.

[24] C.Y. Wong, Singapore, Singapore: World Scientific (1994) 516 p.

[25] H. Satz, Nucl. Phys. A715 (2003) 3, hep-ph/0209181.

[26] E.V. Shuryak, Phys. Rept. 61 (1980) 71.

K. Kajantie and H.I. Miettinen, Zeit. Phys. C9 (1981) 341.

K. Kajantie et al., Phys. Rev. D34 (1986) 2746.

[27] NA50, E. Scomparin et al., Nucl. Phys. A610 (1996) 331c.

HELIOS, M. Masera, Nucl. Phys. A590 (1995) 93c.

[28] R. Rapp and E.V. Shuryak, Phys. Rev. Lett. 86 (2001) 2980, hep-ph/0008326.

[29] T. Matsui and H. Satz, Phys. Lett. B178 (1986) 416.

[30] NA38, C. Baglin et al., Phys. Lett. B220 (1989) 471.

NA50, M.C. Abreu et al., Phys. Lett. B410 (1997) 327.

[31] J. Rafelski and B. Müller, Phys. Rev. Lett. 48 (1982) 1066.

[32] EHS-RCBC Collaboration, J. Bailly et al., Phys. Lett. B 195 (1987) 609.

[33] NA49, M. Gazdzicki et al., (2004), nucl-ex/0403023.

[34] F. Antinori, J. Phys. G30 (2004) S725, nucl-ex/0404032.

[35] L. Van Hove, Phys. Lett. B118 (1982) 138.

L.D. McLerran et al., Phys. Rev. D34 (1986) 2755.

[36] STAR, K.H. Ackermann et al., Phys. Rev. Lett. 86 (2001) 402, nucl-ex/0009011.

[37] M. Gyulassy and M. Plumer, Phys. Lett. B243 (1990) 432.

[38] L.D. Landau and I. Pomeranchuk, Dokl. Akad. Nauk Ser. Fiz. 92 (1953) 535.
A.B. Migdal, Phys. Rev. 103 (1956) 1811.

[39] M. Gyulassy and X.N. Wang, Nucl. Phys. B420 (1994) 583, nucl-th/9306003.
X.N. Wang, M. Gyulassy and M. Plumer, Phys. Rev. D51 (1995) 3436, hep-ph/9408344.

[40] R. Baier et al., Phys. Lett. B345 (1995) 277, hep-ph/9411409.
R. Baier et al., Nucl. Phys. B484 (1997) 265, hep-ph/9608322.

[41] B.G. Zakharov, JETP Lett. 63 (1996) 952, hep-ph/9607440.

[42] X.f. Guo and X.N. Wang, Phys. Rev. Lett. 85 (2000) 3591, hep-ph/0005044.
X.N. Wang and X.f. Guo, Nucl. Phys. A696 (2001) 788, hep-ph/0102230.

[43] M. Gyulassy, P. Levai and I. Vitev, Phys. Rev. Lett. 85 (2000) 5535, nucl-th/0005032.
M. Gyulassy, P. Levai and I. Vitev, Nucl. Phys. B594 (2001) 371, nucl-th/0006010.
U.A. Wiedemann, Nucl. Phys. A690 (2001) 731, hep-ph/0008241.

[44] X.N. Wang, Nucl. Phys. A750 (2005) 98, nucl-th/0405017.

[45] BRAHMS, I. Arsene et al., Phys. Rev. Lett. 91 (2003) 072305, nucl-ex/0307003.

[46] PHENIX, S.S. Adler et al., Phys. Rev. Lett. 91 (2003) 072303, nucl-ex/0306021.

[47] PHOBOS, B.B. Back et al., Phys. Rev. Lett. 91 (2003) 072302, nucl-ex/0306025.

[48] E. Iancu and R. Venugopalan, (2003), hep-ph/0303204.

[49] STAR, J. Adams et al., Phys. Rev. Lett. 91 (2003) 072304, nucl-ex/0306024.

[50] U.A. Wiedemann, (2005), hep-ph/0503119.

[51] R. Baier et al., Phys. Rev. C60 (1999) 064902, hep-ph/9907267.

[52] S. Blyth, Jet study in ultra-relativistic heavy-ion collisions with the ALICE dectector at the LHC, PhD thesis, University of Cape Town, Rondebosch, 7701, South Africa, 2004.

[53] P. Mattig, Phys. Rept. 177 (1989) 141.

[54] X.N. Wang, Z. Huang and I. Sarcevic, Phys. Rev. Lett. 77 (1996) 231.
X.N. Wang and Z. Huang, Phys. Rev. C 64 (1997) 024311.

[55] E.L. Feinberg, Nuovo Cim. A34 (1976) 391.

[56] K. Reygers, Direct-Photon Production from SPS to RHIC Energies, Talk at hard probes 2004, http://agenda.cern.ch./fullAgenda.php?ida=a044573, 2004.

[57] B. Kampfer and O.P. Pavlenko, Z. Phys. C62 (1994) 491.
B. Kampfer and O.P. Pavlenko, Nucl. Phys. A566 (1994) 351c.
M. Strickland, Phys. Lett. B331 (1994) 245.

[58] R.C. Hwa and K. Kajantie, Phys. Rev. D32 (1985) 1109.

[59] J.I. Kapusta, P. Lichard and D. Seibert, Phys. Rev. D44 (1991) 2774.

[60] L. Xiong, E.V. Shuryak and G.E. Brown, (1992), Prepared for Particles & Fields 92: 7th Meeting of the Division of Particles Fields of the APS (DPF 92), Batavia, Illinois, 10-14 Nov 1992.

[61] P. Arnold, G.D. Moore and L.G. Yaffe, JHEP 12 (2001) 009, hep-ph/0111107.
J.P. Blaizot and F. Gelis, (2005), hep-ph/0504144.

[62] S. Turbide, R. Rapp and C. Gale, Int. J. Mod. Phys. A19 (2004) 5351, hep-ph/0408119.

[63] C. Gale, (2005), hep-ph/0504103.

[64] R.J. Fries, B. Muller and D.K. Srivastava, Phys. Rev. Lett. 90 (2003) 132301, nucl-th/0208001.

[65] B.G. Zakharov, JETP Lett. 80 (2004) 617, hep-ph/0410321.

[66] S. Frixione, Phys. Lett. B429 (1998) 369, hep-ph/9801442.

[67] WA98, M.M. Aggarwal et al., Phys. Rev. Lett. 85 (2000) 3595, nucl-ex/0006008.

[68] PHENIX, S.S. Adler et al., (2005), nucl-ex/0503003.

[69] PHENIX, J. Frantz, J. Phys. G30 (2004) S1003, nucl-ex/0404006.

[70] F. Arleo et al., (2003), hep-ph/0311131, CERN Yellow Report, CERN-2004-009.

[71] M. Werlen and H. Delagrange, Private Communication, 2005.

[72] F. Arleo et al., JHEP 11 (2004) 009, hep-ph/0410088.

[73] http://athome.web.cern.ch/athome/lhc/lhc.html.

[74] http://edms.cern.ch.

[75] I. Glässel, Talk at Quark Matter 2004, Oakland, USA, 2004.

[76] W. Leo, Techniques for Nuclear and Particle Physics Experiments (Springer-Verlag, 1987).

[77] R. Wigmans, Calorimetry, Energy Measurements in Particle Physics (Clarendon Press, Oxford, 2002).

[78] R. Brun and F. Rademakers, Proceedings AIHENP'96 Workshop, Lausanne, Sep. 1996 Vol. 389, pp. 81–86, 1997, See also http://root.cern.ch.

[79] T. Sjöstrand et al., Computer Phys. Commun. 135 (2001) 238.

[80] X.N. Wang and M. Gyulassy, Computer Phys. Commun 83 (1995) 307.

[81] CERN, GEANT - Detector Description and Simulation Tool, 1993, Available at http://wwwinfo.cern.ch/asdoc/geant_html3/geantall.html.

[82] L. Betev et al., (2003), ALICE-INT-2003-038.

[83] B. Andersson et al., Phys. Rept. 97 (1983) 31.

[84] PHOBOS, B.B. Back et al., Phys. Rev. C65 (2002) 061901, nucl-ex/0201005.

[85] G.A. Akopdjanov et al., Nuclear Instruments and Methods 140 (1977) 441, http://www.sciencedirect.com/science/article/B73DN-471XFCS-Y6/2/c6e753227616aaff934c48cf7b327fad.

[86] T. Awes et al., Nuclear Instruments & Methods in Physics Research A311 (1992) 130.

[87] F. Berger et al., Nuclear Instruments & Methods in Physics Research A321 (1992) 152.

[88] . The ALICE Collaboration, The ALICE Physics Performance Report (2004).

[89] C.N. Chou, Phys. Rev. 87 (1952) 904.

[90] J. Birks, The theory and practice of scintillation counting (Macmillan, 1964).

[91] R. Craun and D. Smith, Nuclear Instruments and Methods 80 (1970).

[92] M. van Leeuwen, Private Communication.

[93] I. Johnson, Quark matter 2002. Proceedings, 16th International Conference on ultra-relativistic nucleus nucleus collisions, edited by H. Gutbrod, J. Aichelin and K. Werner Vol. 715, pp. 691–694, 2003.

[94] A. Wetzler, Private Communication.

[95] M. Horner, Private Communication.

[96] A. Morsch, Private Communication.

[97] F. Carminati, Private Communication.

[98] A. Fasso et al., Proceedings of the MonteCarlo 2000 Conference Lisbon, pp. 955–960, 2000, See also http://www.fluka.org.

[99] S. Blyth, Private Communication.

[100] J. Letessier and J. Rafelski, Hadrons and Quark-Gluon Plasma (Cambridge University Press, 2002).